Late Oligocene high-temperature shear zones in the core of the Higher Himalayan Crystallines (Lower Dolpo, western Nepal)

R. Carosi,[1] C. Montomoli,[1] D. Rubatto,[2] and D. Visonà[3]

Received 2 October 2008; revised 20 November 2009; accepted 13 January 2010; published 25 August 2010.

[1] A high-temperature shear zone, Toijem shear zone, with a top-to-the-SW sense of shear affects the core of the Higher Himalayan Crystallines (HHC) in western Nepal. The shear zone developed during the decompression, in the sillimanite stability field, of rocks that previously underwent relatively high-pressure metamorphism deformed under the kyanite stability field. PT conditions indicate that the footwall experienced higher pressure (~9 kbar) than the hanging wall (~7 kbar) and similar temperatures (675°–700°C). Monazite growth constrains the initial activity of the shear zone at 25.8 ± 0.3 Ma, before the onset of the Main Central Thrust zone, whereas the late intrusion of a crosscutting granitic dike at 17 ± 0.2 Ma limits its final activity. Monazites in kyanite-bearing gneisses from the footwall record prograde metamorphism in the HHC from ~43 to 33 Ma. The new data confirm that exhumation of the HHC started earlier in western Nepal than in other portions of the belt and before the activity of both the South Tibetan Detachment System (STDS) and Main Central Thrust (MCT) zones. As a consequence, western Nepal represents a key area where the channel-flow-driven mechanism of exhumation, supposed to be active from Bhutan to central-eastern Nepal, does terminate. In this area, exhumation of crystalline units occurred by foreland propagation of ductile and, subsequently, brittle deformation. **Citation:** Carosi, R., C. Montomoli, D. Rubatto, and D. Visonà (2010), Late Oligocene high-temperature shear zones in the core of the Higher Himalayan Crystallines (Lower Dolpo, western Nepal), *Tectonics*, *29*, TC4029, doi:10.1029/2008TC002400.

1. Introduction

[2] The Himalayan mountain belt, developed during the India-Asia collision since ~55 Ma, is regarded as a classic collisional orogen. It is characterized by the impressive continuity over hundreds of kilometers of tectonic features such as thrusts and normal faults, as well as large volumes of high-metamorphic grade rocks and granite exposed at the surface. This constitutes an invaluable field laboratory to unravel the tectonic and metamorphic evolution of crystalline units and the mechanisms of exhumation of deep-seated rocks in orogens.

[3] Low-angle normal faults are among the most prominent exhumation features preserved in the Himalaya. The South Tibetan Detachment System (STDS) at the top of the HHC in central and eastern Nepal was recognized early [*Caby et al.*, 1983] as a system of low-angle normal faults. Their contemporaneous activity with the shortening along the Main Central Thrust (MCT) at its base [*Burchfiel and Royden*, 1985; *Burg et al.*, 1984; *Burchfiel et al.*, 1992; *Hodges et al.*, 1993; *Brown and Nazarchuk*, 1993; *Coleman*, 1996; *Carosi et al.*, 1998, 1999; *Searle*, 1999; *Godin et al.*, 1999] led to the development of new models for the exhumation and extrusion or channel flow of crystalline rocks [e.g., *Burchfiel et al.*, 1992; *Edwards et al.*, 1996; *Grasemann et al.*, 1999; *Grujic et al.*, 2002; *Beaumont et al.*, 2001; *Daniel et al.*, 2003; *Catlos et al.*, 2004]. These models bear on our understanding of the tectonic and metamorphic evolution of the Himalayan belt, which has implications for the evolution of other ancient and recent orogens [*Chemenda et al.*, 1995; *Hatcher and Merschat*, 2006].

[4] The activity of the main structural discontinuities in the Himalayas, such as the MCT and the STDS, is bracketed mainly between 23 and 17 Ma [*Hodges*, 2000, and references therein] (central-western Nepal: *Godin et al.*, 2006]). Although the later tectonic and metamorphic history of the HHC is well constrained, very few data are available on the long period spanning the onset of collision and the initial stages of extrusion at ~23 Ma. In this study we present new structural, petrological, and geochronological results for the HHC of western Nepal (Figures 1 and 2), documenting a previously unrecognized high-temperature shear zone in the core of the HHC. U-Th-Pb monazite ages from a mylonite record the oldest shear zone documented in the crystalline unit. We propose that its earlier activity played a primary role in the exhumation, decompression, and partial melting of the HHC, before the onset of exhumation by the activity of the MCT-STDS system localized along its tectonic boundaries.

2. Geological Setting

[5] In the Nepal Himalaya four main tectonic units, separated by tectonic discontinuities, are found [*Gansser*, 1964; *Le Fort*, 1975; *Lombardo et al.*, 1993; *Upreti*, 1999; *Hodges*, 2000; *Yin*, 2006] (Figure 1) that from top to bottom are

[1]Dipartimento di Scienze della Terra, University of Pisa, Pisa, Italy.
[2]Research School of Earth Sciences, Australian National University, Canberra, Australia.
[3]Dipartimento di Geoscienze, University of Padova, Padova, Italy.

0278-7407/10/2008TC002400

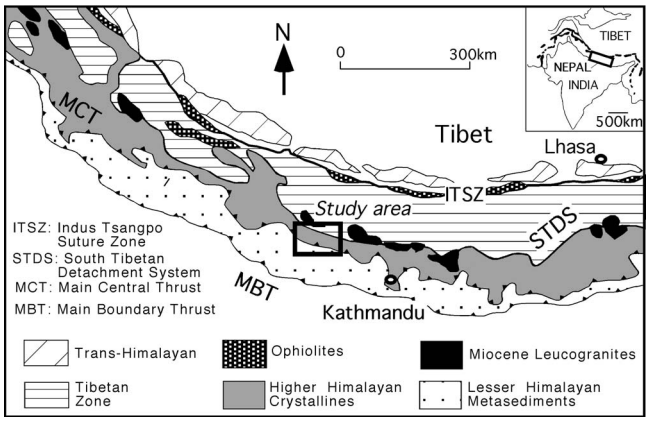

Figure 1. Geological sketch map of Himalayas, with location of study area.

the Subhimalayan, the Lesser Himalayan (LH), the Higher Himalayan Crystallines (HHC), and the Tibetan Sedimentary Sequence (TSS).

[6] The Subhimalayan unit is made up by a Tertiary molasse (Siwalik Group) [*DeCelles et al.*, 1998] deposited in a foreland basin formed by flexural downwarping of the Indian plate beneath the Himalayan load. The Lesser Himalaya is composed of a thick sequence of low-grade or unmetamorphosed [*Beyssac et al.*, 2004] Precambrian to Eocene cover rocks and by higher-grade metamorphic rocks (Lower Himalayan Crystalline Nappes [*Fuchs*, 1964, 1977; *Fuchs and Frank*, 1970]).

[7] The LH is separated from the lower and upper tectonic units by the Main Boundary Thrust (MBT) and the MCT, respectively, both showing a top-to-the-SW sense of movement. The Main Central Thrust in Lower Dolpo corresponds to a wide zone (thickness 1–4 km) of mylonitic deformation [*Carosi et al.*, 2007]. An inverted metamorphic field gradient has been confirmed on both the meso- and microscales in the MCT zone [*Harrison et al.*, 1999, and references therein].

[8] The contact between the LH and the overlying Higher Himalayan Crystallines, mapped by *Fuchs and Frank* [1970], broadly corresponds to the Ramgarh thrust [*Larson and Godin*, 2009]. According to some other authors, the Ramargh thrust is totally confined in the LH [*DeCelles et al.*, 2001; *Robinson et al.*, 2003, 2006].

[9] The Higher Himalayan Crystallines are made up of a thick sequence of metasedimentary and metaigneous rocks, from Neoproterozoic to Ordovician in age [*Hodges*, 2000], represented by pelitic paragneisses, metacarbonate rocks, calcschists, granitic orthogneisses, and migmatites. The unit has been deformed under medium- and high-grade metamorphic conditions [*Lombardo et al.*, 1993; *Le Fort*, 1994]. The upper portion of the unit is intruded by abundant Miocene leucogranites [*Guillot et al.*, 1999; *Hodges*, 2000].

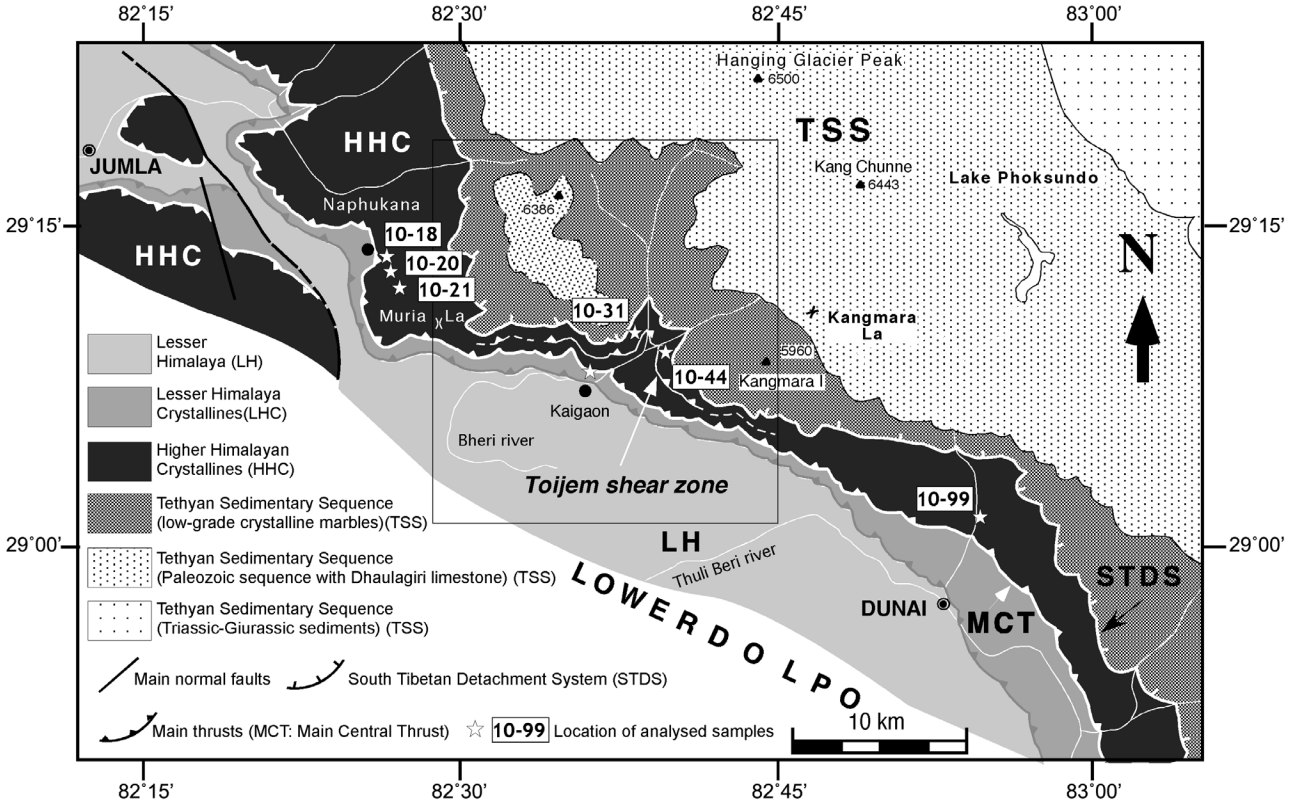

Figure 2. Geological map of Dolpo area in western Nepal [after *Carosi et al.*, 2007]. Box is the area shown in Figure 5.

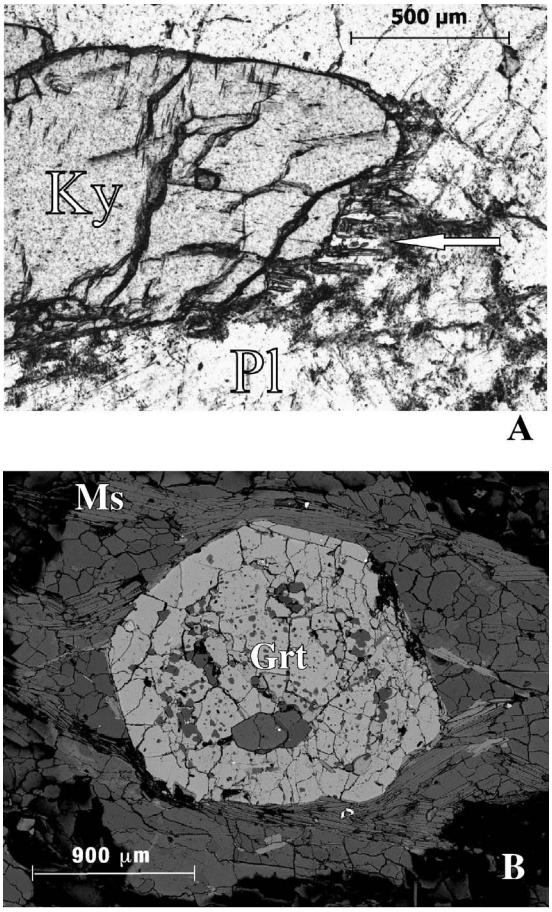

Figure 3. Microtextures in paragneisses from unit 1. (a) Kyanite-bearing gneiss with kyanite crystals elongated along S_2 foliation. Growth of small beards of sillimanite and kyanite detected by Raman spectroscopy indicated by white arrow. (b) BSE image of garnet crystal, wrapped in foliation (S_2) defined by muscovite and biotite. Garnet shows large poikilitic core and inclusion-free rim. Mineral abbreviations are according to *Kretz* [1983].

[10] The Tethyan Sedimentary Sequence crops out above the HHC. It comprises a nearly continuous sequence of lower Paleozoic to Eocene sediments which were deposited on the northern passive margin of the Indian plate [*Gaetani and Garzanti*, 1991]. The sequence was deformed under very low grade metamorphic conditions [*Crouzet et al.*, 2007].

[11] In western Dolpo, the lowest part of the TSS is represented by the Cambrian (?)–Ordovician Dhaulagiri Limestone that registers both the highest metamorphic grade and strain [*Carosi et al.*, 2007]. The main lithotype is represented by biotite-bearing marbles that show a complex and penetrative deformation [*Carosi et al.*, 2007]. The TSS also contains plutons of biotite-muscovite granites, the North Himalayan granites, which were emplaced during the Miocene [*Guillot et al.*, 1999]; in the carapaces of the domes the highest metamorphic conditions have been registered [*Lee et al.*, 2000]. The South Tibetan Detachment System is constituted by a brittle-ductile top-to-the-North shear zone that divides the TSS from the HHC and is active from 23 to 17 Ma [*Godin et al.*, 2006].

3. Higher Himalayan Crystallines

[12] Across the Himalayan chain west of Bhutan, the HHC is composed of three main portions (named formations 1, 2, and 3 by *Le Fort* [1975] and units 1, 2 and 3 by *Searle and Godin* [2003]) which show impressive lateral continuity. The only notable variations are the thickness of the crystalline unit varying from ~30 km in the Bhutan Himalayas to ~2–4 km in western Nepal (Figure 2) [*Carosi et al.*, 2002; *Godin et al.*, 2006] and the volume of the Miocene leucogranites, which are not homogeneously distributed along the strike.

[13] In the study region, unit 1 is made up of (centimeter-size) kyanite and garnet-bearing paragneisses (Figure 3) and micaschists with thin levels of calc-silicates and boudins of garnet-bearing amphibolites. The metamorphic assemblage in gneisses and micaschists is quartz + biotite + muscovite + garnet + staurolite + kyanite I ± plagioclase with accessory tourmaline, Fe-Ti oxides, rutile, apatite, zircon, monazite, and U-Th oxides. Prismatic sillimanite is found only at the top of unit 1 approaching unit 2; in the other rocks, acicular/fibrous sillimanite is elongated parallel to the S_2 foliation, around garnet poikiloblasts or kyanite crystals armored by retrograde muscovite. Muscovite and biotite are also elongated parallel to the foliation and represent retrograde greenschist facies metamorphism.

[14] White marbles, calc-silicate gneiss, with minor amounts of pelitic and psammitic rocks, constitute unit 2. The observed assemblages in marble and calc-silicate gneiss (quartz + plagioclase ± k feldspar + clinopyroxene + epidote + scapolite + garnet + biotite + muscovite ± calcite ± hornblende, with accessory tourmaline, rutile, titanite, apatite, zircon, and Fe-Ti oxides) are consistent with the kyanite-grade metamorphism of the associated metapelites.

[15] Unit 3 is composed of orthogneiss and migmatitic gneisses. The latter, which host intercalations of calc-silicates, usually contain the assemblage quartz ± plagioclase ± k feldspar + clinopyroxene + epidote + scapolite + garnet + biotite + muscovite ± calcite ± hornblende with accessory tourmaline, rutile, titanite, apatite, zircon, and Fe-Ti oxides [*Carosi et al.*, 2002]. Calc-silicate-bearing marbles, occurring at the top of the unit (thickness ~ 0.5–1 km), contain the amphibolite facies assemblage tremolite + calcite + diopside ± quartz, retrogressed to the greenschist facies assemblage tremolite + calcite ± scapolite ± biotite ± quartz.

[16] A network of leucogranite sills and dikes intrude in unit 3 showing increasing deformation (from undeformed to stretched and folded) approaching the STDS zone. Spectacular exposure of deformed dikes can be observed south of Kangmara and Triangle Peak, and on the right bank of the Panipatta Khola (Figure 2). The dikes, several hundred meters in length, are tightly folded perpendicularly to the main fabric, and stretched and boudinaged parallel to it. Approaching the STDS, these dikes progressively rotated parallel to the main fabric. Similar dikes have been dated at

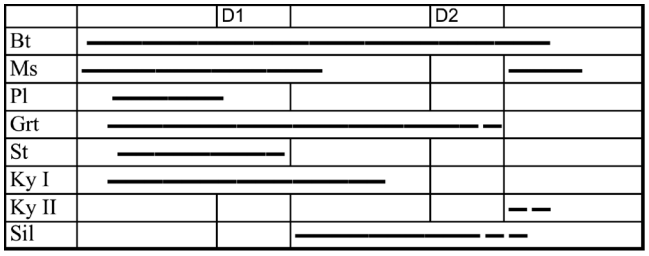

Figure 4. Relations between mineral growth and D_1 and D_2 deformation phases in units 1 and 2 of HHC. Mineral abbreviations are according to *Kretz* [1983].

~ 23 Ma by *Godin et al.* [2001] in the Kali Gandaki region (west of the Annapurna Range).

[17] The main fabric in the HHC is a foliation formed during a second deformation phase (S_2; [*Carosi et al.*, 1999, 2007]). It is often recognizable as a shear band cleavage as defined by *Passchier and Trouw* [1996]. The S_2 foliation strikes NW-SE and dips 30°–60° toward the NE. It is marked by the preferred orientation of metamorphic minerals and recrystallized quartz ribbons. Kyanite, staurolite, muscovite, and biotite are occasionally bent or kinked along shear bands (Figure 4). Top-to-the-SW sense of shear is marked by C-S fabric, shear bands, asymmetric tails around porphyroclasts, and rotated garnets within the mylonites in the lower portion of the HHC. The elongation lineation (L_2) trends N020E to N040E and plunges NE moderately to steeply (20°, 60°). S_1, formed during D_1 deformation is sometimes preserved as a relict in D_2 fold hinges (F_2) and S_2 microlithons and as internal foliation in porphyroblasts.

[18] The HHC underwent at least two later folding phases, characterized by nearly orthogonal NW-SE and NE-SW trending fold axes, causing kilometer-scale open folds with steeply dipping axial planes. These folds affect the tectonic boundaries (see geological cross sections in *Upreti* [1999] and *Carosi et al.* [2002, 2007]) and are a large-scale feature, since they have also been described eastward in the Annapurna Range [*Godin et al.*, 2001] and in the Mt. Everest-Mt. Makalu region [*Lombardo et al.*, 1993; *Carosi et al.*, 1999; *Schelling*, 1999].

4. High-Temperature Shear Zone: Toijem Shear Zone

[19] A 40–50 m thick ductile shear zone (Toijem shear zone: TSZ) was identified in the kyanite- and sillimanite-bearing gneisses of the HHC (Figure 5), on the basis of detailed field and structural mapping. The TSZ crops out in the Garphung Khola at an altitude of 3300 m (Figure 5). The mylonites are located in the upper part of the Unit 1 gneisses near the contact with the overlying gneisses and high-grade marbles of Unit 2. The TSZ does not cause a repetition of the units in the HHC, as observed elsewhere in the HHC [*Gruijc et al.*, 2002].

[20] The mylonites show augens and microlithons consisting of garnet + plagioclase + quartz + kyanite and muscovite (Figure 6). The mylonitic foliation is defined by biotite, muscovite, prismatic sillimanite, quartz, and plagioclase. Shear planes strike N110E to N120E and dip moderately to the NE (40°–45°) (Figure 5 inset). Mineral lineation, marked by garnet, quartz, sillimanite, and biotite, or by tails around millimeter- to centimeter-size feldspar porphyroclasts, trends N045E and plunges 30°–40° to the NE (Figure 5 inset). The sense of shear, deduced from shear band cleavages, mica fishes, and rotated porphyroclasts is top-to-the-SW (Figure 6).

[21] SW-verging tight to isoclinal folds, with axes trending nearly N050E and plunging steeply to the SW, are crosscut by shear planes. These folds transpose the main fabric in the HHC and are thus regarded as F_2 folds, developed during an earlier stage of movement of the TSZ, which rotated the fold axes parallel to the lineation.

[22] The hanging wall of the TSZ is made up by units 2 and 3. Leucogranite dikes and sills occur exclusively in the hanging wall of the TSZ, where they are stretched and folded, showing deformation at different stages of emplacement. Leucogranite dikes crop out near the Toijem police station (Figures 5 and 7) and crosscut, at a high angle, the mylonitic foliation of the TSZ. They are weakly foliated. Microscopically, the foliation is defined by rounded plagioclase, quartz, and biotite. However, the dikes recorded less strain with respect to the TSZ mylonites. This implies that most of the deformation within the TSZ occurred before the intrusion of the dikes; only the latest increments were recorded.

[23] The footwall of the TSZ is made up of paragneisses and micaschists, with rare marbles and calc-silicate levels. In the pelites, thin mica layers (biotite + muscovite) define the main foliation around garnets and kyanite porphyroclasts, muscovite fishes, and polycrystalline quartz aggregates. Garnet is pecilitic with cores rich in small inclusions aligned along an internal foliation, discordant with respect to the external foliation. Kyanite and plagioclase are commonly deformed and fractured. Secondary needles of kyanite occasionally grow perpendicular to prismatic kyanite. Prismatic sillimanite also occurs in the TSZ mylonites, along shear planes associated with biotite, plagioclase, quartz, and muscovite (Figure 6d) and sometimes is armored by biotite and muscovite, but never in direct association with kyanite.

5. Petrography and PT Estimates

[24] Nearly 120 samples were collected for microstructural analysis covering the three main tectonic units of the area. Seven fresh and representative samples of the HHC were selected for petrography and PT estimates (Figure 2), including gneiss from the footwall of the TSZ (samples 10–18, 10–20, 10–21, 10–99), mylonite within the TSZ (samples 10–43, 10–44), and a leucogranite dike intruding into the hanging wall of the TSZ (sample 10–31). Four of the samples containing abundant monazite and zircon were subjected to geochronological analysis.

[25] Estimates of P-T conditions recorded by gneisses and micaschists were evaluated with garnet-biotite thermometer [*Bhattacharya et al.*, 1992] Grossular + 2Kyanite/Sillimanite + Quartz = 3Anorthite (Garnet-Aluminosilicate-Quartz-Plagioclase: GASP geobarometer) and Grossular +

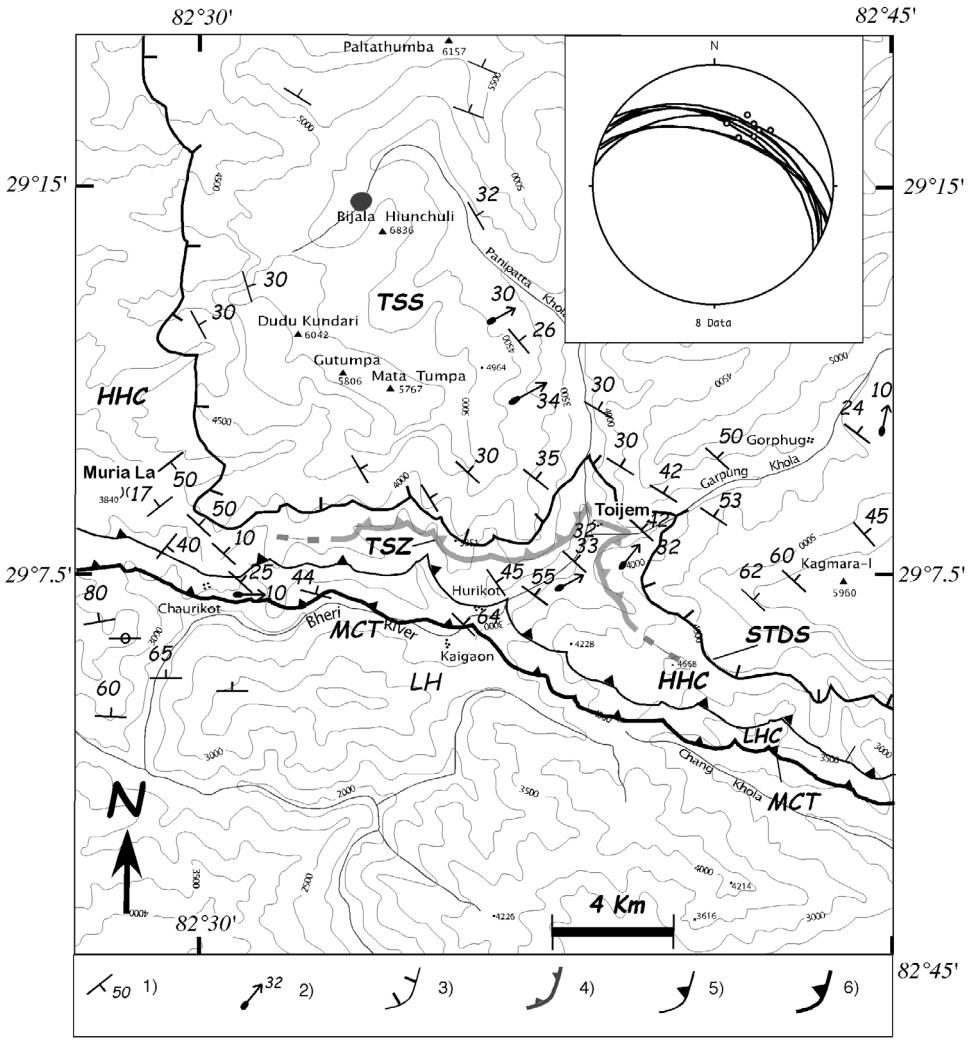

Figure 5. Structural map of Lower Dolpo area west of Kangmara Peak. LH, Lesser Himalaya; LHC, Lesser Himalayan Crystallines; HHC, Higher Himalayan Crystallines; TSS, Tethyan Sedimentary Sequence; MCT zone, Main Central Thrust zone; 1, main foliation; 2, elongation lineation; 3, South Tibetan Detachment System (STDS); 4, Toijem Shear Zone (TSZ); 5, Main Central Thrust (MCT); 6, thrust of LHC over LH sequence. Topographic map redrawn from Nepa Maps by P. Gondoni, scale 1:135000. Inset is a stereographic projection of structural elements of Toijem Shear Zone: shear planes (great circles) and object lineations (dots).

Almandine + Muscovite = 3Anorthite + Annite (GPMP-Fe geobarometer) [*Holland and Powell*, 1998] (data set calibrations). The analytical conditions used for PT estimates are described in Appendix A. The results are shown in Table 1, with a pressure error within ±100 MPa and a temperature error within ±25°C [*Hoisch*, 1990; *Spear*, 1993].

[26] In the TSZ footwall, the assemblage included in the garnet of the metapelites gave temperatures between 575 and 602°C and pressures between 636 and 796 MPa (GASP barometer). Significantly higher values were obtained from minerals in the matrix and in equilibrium with garnet rims: T = 643°–665°C and P = 745–896 MPa. Evolution toward higher pressures and temperatures matches the occurrence of staurolite within garnet porphyroblasts, which implies the prograde breakdown of staurolite to garnet.

[27] Similarly, in the TSZ mylonites, increasing temperature and pressure values were recorded from garnet core to rim (core T = 585°–614°C, P = 566–602 MPa; rim T = 618°–676°C, P = 625–702 MPa). Pressure values are lower than in the footwall, fitting the observation that kyanite is replaced by sillimanite at the temperature peak.

[28] The P and T values obtained in this work (Figure 8) generally match those previously reported for the HHC in the adjoining Dhaulalgiri-Annapurna areas [*Vannay and Hodges*, 1996], Langtang [*Inger and Harris*, 1993; *Macfarlane*, 1995; *Fraser et al.*, 2000; *Catlos et al.*, 2002], and central-eastern

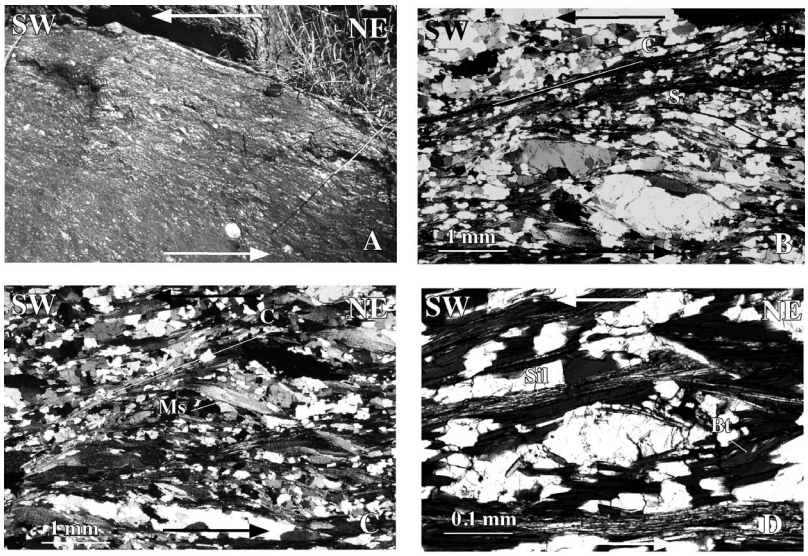

Figure 6. Structures in Toijem Shear zone. Top-to-the-SW sense of shear in all pictures. (a) Outcrop view of mylonite. Lens cap diameter: 5.2 cm. (b) Photomicrograph showing C-S fabric within shear zone. (c) Photomicrograph of mica fishes. (d) Photomicrograph of sillimanite and biotite growing along mylonitic foliation.

Himalaya [e.g., *Swapp and Hollister*, 1991; *Guillot*, 1999; *Borghi et al.*, 2003]. However, we obtained two distinct P-T paths for the TSZ and its footwall (Figure 8). The thermobarometric data suggest a prograde path for both footwall rocks and mylonite in the kyanite and sillimanite field, respectively (Figure 8). The metamorphic peak was followed by decompression in the sillimanite field for the mylonites (B in Figure 8) and at the sillimanite-kyanite boundary for the footwall rocks (A in Figure 8), as indicated by the presence of retrograde kyanite and sillimanite. According to the above P-T path (A in Figure 8), the footwall rocks of the TSZ did not reach the field of dehydration melting of staurolite for metapelites at 500 MPa [*Spear et al.*, 1999]. The shaded area in Figure 8 corresponds to the stable field for the assemblage staurolite + garnet + biotite found in the HHC metapelites north of Makalu [*Borghi et al.*, 2003]. Unlike the footwall, the P-T path for the mylonites (path B in Figure 8) intersects the dehydration melting curve for staurolite.

[29] The two different P-T paths match the occurrence of staurolite, as both single-phase mineral and as relicts included in garnets and in metapelites. Staurolite melting in the TSZ mylonites may explain the presence of leucogranite only above the TSZ. The small amount of granite observed in the study area may be due to low-melt generation in the pelites, which did not reach muscovite + albite dehydration melting [*Harris and Massey*, 1994; *Harris et al.*, 1995; *Scaillet et al.*, 1995; *Thompson*, 1996; *Spear et al.*, 1999].

6. U-Pb Geochronology

[30] Geochronology was conducted in four samples from various tectonic positions to constrain the timing of movements along the TSZ (see Figure 2 for locations and Table 2 for description of samples). The samples are two kyanite-bearing gneiss from the lower part of the HHC, in the footwall of the TSZ (samples 10–20, 10–99), a sillimanite- and kyanite-bearing mylonite from within the TSZ (sample 10–44), and the leucogranitic dike from the hanging wall of the TSZ (sample 10–31).

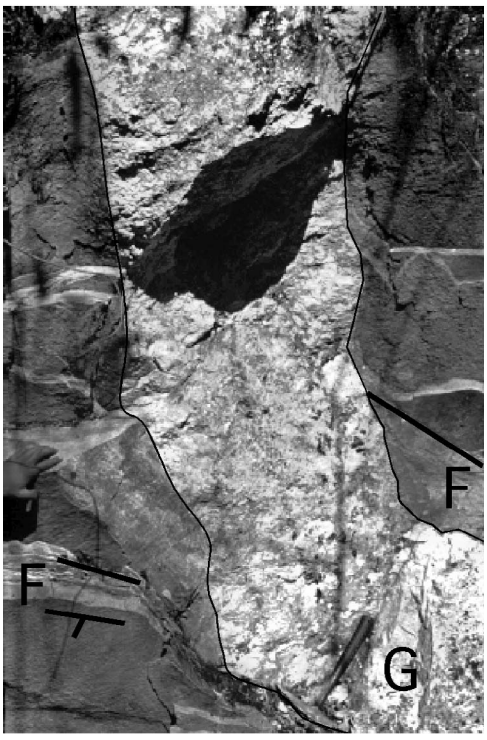

Figure 7. Leucogranite dike (G) (location of sample 10–31) crosscutting mylonitic foliation (F) in marble of unit 2. Locality: Panipatta Khola (see Figures 2 and 5).

Table 1. Results of Thermobarometric Calculations[a]

Sample	Biotite		Muscovite		Garnet			Pl	P (Mpa)		T (°C)
	Xfe	XMg	Xfe	XMg	XMn	XCa	FM	Xan	GASP	GPMP-Fe	Grt-Bt
D10-18											
(core + inclusions)	0.322	0.678	0.381	0.619	0.007	0.020	0.720	0.068	636	750	575
(rim + matrix)	0.401	0.559	0.372	0.628	0.011	0.024	0.731	0.072	848	818	665
D10-20											
(core + inclusions)	0.409	0.591	0.643	0.357	0.019	0.028	0.752	0.066	796	811	602
(rim + matrix)	0.492	0.508	0.647	0.353	0.025	0.028	0.761	0.068	896	833	652
D10-21											
(rim + matrix)	0.450	0.550	0.343	0.657	0.029	0.041	0.729	0.147	745	738	643
D10-43											
(core + inclusions)	0.470	0.530	0.567	0.413	0.050	0.019	0.777	0.081	566	606	585
(rim + matrix)	0.452	0.548	0.551	0.449	0.048	0.020	0.780	0.094	639	609	643
D10-44											
(rim + matrix)	0.473	0.527	0.664	0.336	0.142	0.057	0.644	0.252	625	550	618
D10-99											
(core + inclusions)	0.458	0.542	0.462	0.538	0.045	0.022	0.753	0.102	602	607	614
(rim + matrix)	0.508	0.492	0.554	0.446	0.040	0.022	0.743	0.105	702	652	676

[a]Estimated errors are ±100 MPa for pressure and ±25°C for temperature [*Hoisch*, 1990; *Spear*, 1993].

6.1. Monazite Geochronology

[31] Analytical methods for U-Th-Pb monazite geochronology are described in Appendix B. Gneiss samples 10–20 and 10–99 contain small (20–100 μm diameter) monazite crystals included in both garnet and matrix (Figure 9). Analysis was performed on polished thin sections to preserve textural relationships. Backscattered electron (BSE) imaging of monazite did not reveal any zoning.

[32] In sample 10–20, monazite grains in the matrix as well as monazite included in garnet were analyzed: 10 analyses on monazite included in garnet and 5 analyses on matrix monazite. Apparent U-Pb ages range between 43.5 ± 0.5 and 28.8 ± 0.3 Ma in garnet alone. The oldest age component, at ~43 Ma, was only found in monazite included in garnet (three analyses at 42.6 ± 2.1 Ma; Figure 9). At least in one garnet, the 44 Ma monazites are found as inclusions in the core, which has a higher Ca content (see map of garnet B in Figure 9). Monazites in the matrix yielded ages scattered between ~ 39.6 and 30.8 Ma (Figure 10a, Table 3). Considering all ages, the major peak is at ~39 Ma (six analyses at 39.0 ± 0.6 Ma) and comprises equally inclusions in garnet and matrix monazite (Figures 9 and 10). Another cluster, at ~33 Ma (four analyses at 32.7 ± 1.0 Ma), again includes monazite in both textural settings. It is noteworthy that there is no correlation between age and variations in the concentration of Th-U or other trace element (see below).

[33] Sample 10–99 has a texture similar to that of gneiss 10–20, with the difference that monazite is more abundant in the matrix than in garnet. Three crystals were dated in sample 10–20 (five analyses in total, Table 3), two of which are in the matrix. The monazite included in garnet yielded the oldest ages at 47.7 ± 0.3 and 38.05 ± 0.24 Ma. The matrix ages are scattered at ~39, ~32, 25, and 22 Ma (Figure 10a).

[34] The monazite from mylonite sample 10–44 was analyzed as separate grains mounted in epoxy. The grains are between 50 and 200 μm across, rounded to anhedral, light yellow, and transparent; one third of the grains recovered were crystal fragments. Under BSE, a variety of zoning patterns from broad-banded oscillatory sector, patches, and unzoned domains were observed (Figure 11). It was concluded that two to three concentric zones exist in a few crystals. The 34 measured $^{206}Pb/^{238}U$ ages range between 16.5 ± 0.3 and 29.6 ± 0.4 Ma and cannot be easily correlated

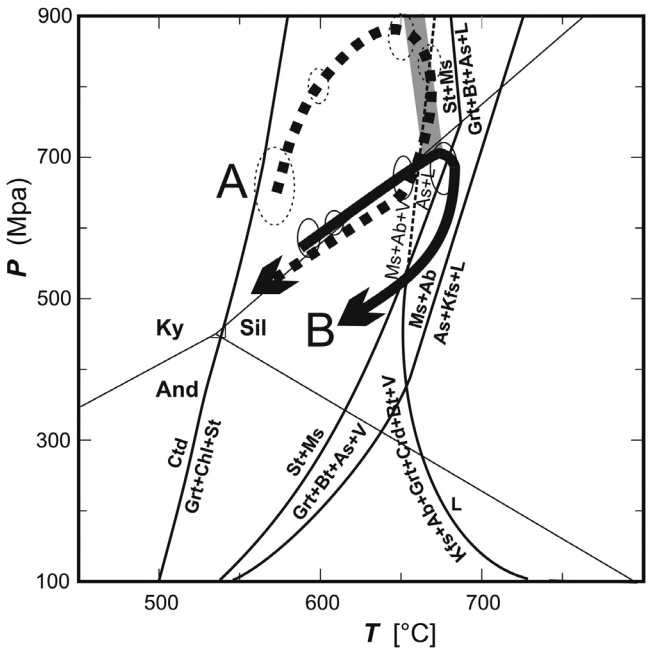

Figure 8. Calculated P-T-t path for rocks of footwall (a) and hanging wall (b) of Toijem Shear Zone. Grey band at top of graph corresponds to stable field for staurolite + garnet + biotite assemblage [from *Borghi et al.*, 2003]. Al_2SiO_5 phase relations after *Pattison* [1992]; muscovite + albite and muscovite + staurolite stability are from *Spear et al.* [1999]; chloritoid and garnet + chlorite + staurolite stability is from *Wei et al.* [2004]. Ellipses indicate errors in the measurements.

Table 2. Description of Samples Used for U-Th-Pb Geochronology Analysis

Sample	Lithology	Structure	Foliation	Mineral Assemblage	Accessory Minerals	Foliation's Minerals	Notes
10–20	Gneiss	Augen	Coarse continuous foliation	Quartz, muscovite, garnet, plagioclase, staurolite, kyanite, biotite	Ilmenite, rutile, tormaline, zircon, monazite	Muscovite, biotite, quartz, plagioclase, quartz ribbons	Small beards of sillimanite occur in strain fringes around kyanite
10–99	Gneiss	Augen	Coarse continuous foliation	Quartz, muscovite, garnet, plagioclase, staurolite, kyanite, biotite	Ilmenite, rutile, tormaline, zircon, monazite	Muscovite, biotite, quartz, plagioclase, quartz ribbons	
10–44	Mylonitic micaschists	Mylonites with mm-size porphyroclasts	S-C fabric	Garnet, plagioclase, quartz, kyanite, muscovite	Tourmaline, Fe-Ti oxides, rutile, apatite, zircon, monazite and uraninite/thorite	Biotite, muscovite, sillimanite, minor quartz and plagioclase	Garnet with large pecilitic cores and inclusion-poor rims. Internal foliation made by quartz, plagioclase, biotite, rutile, apatite, zircon, monazite, uraninite/thorite
10–31	Two-mica lucogranite dike	Fine to medium - grained, weakly oriented	Coarse, weak	Quartz, plagioclase, k-Feldspar, biotite, muscovite, tourmaline	Zircon, apatite, monazite, Fe-Ti oxide	Plagioclase, quartz, biotite	Biotite blades sometimes define a weak foliation

to zoning (Figure 11). Textural relationships within one grain are generally respected, cores being older than the rims or of the same age. However, cores in different grains sometimes yielded significantly different ages. Age scattering presents some discrete peaks (Figure 10a and Table 3): the major cluster is defined by 11 analyses with an average of 25.8 ± 0.3 Ma (MSWD 1.9 Ma); minor peaks are present at ~16.5 Ma ($N = 3$), 19.9 Ma ($N = 4$), and 28.3 Ma ($N = 3$).

[35] Sample 10–31, a granitic dike, contains zircon and monazite, but the zircon does not have sufficiently large metamorphic rims and thus was not considered for geochronology. Monazite crystals are similar to those of sample 10–44. Their internal zoning is characterized by weak oscillatory zoning (Figure 11), with a few crystals having a BSE-bright rim, which was never large enough to be dated. A smaller monazite population is rich in inclusions, is smaller in size, and has patchy BSE zoning. Unfortunately, its small size, the inclusions, and the extremely high common Pb content all make it impossible to date the inclusion-rich monazite. Analyses of oscillatory zoned monazite gave constantly high U and Th contents (Table 3), with a tight cluster of ages at 17.6 ± 0.2 Ma (MSWD 2.0, Figure 10b).

6.2. Trace Element Chemistry (Sample 10–20)

[36] In gneiss sample 10–20, the overlap of monazite ages in matrix and garnet indicate that textural relationships alone cannot be relied upon to determine the relative timing of these two minerals. In previous studies, trace elements have been proved to be a useful tool for relating accessory monazite growth to the formation of major minerals, in particular, garnet, mainly by using Y and REE abundance and partitioning [e.g., *Foster et al.*, 2000; *Hermann and Rubatto*, 2003; *Kohn et al.*, 2005], Therefore, we investigated the trace element chemistry of the various monazite generations and garnet (Figure 12). LA-ICPMS trace element analyses of monazite (diameter 19μm) were overlapped with existing SHRIMP pits (~20 μm).

[37] The large garnets of sample 10–20 have variable trace element composition from core to rim, with several elements (P, Ti, Y, Zr, and HREE) varying over 1 order of magnitude or more. Profiles across the two garnet crystals do not match a bell-shape zoning and are not necessarily similar, even though they show comparable variations in the concentrations of elements (Figure 12a). Chondrite-normalized patterns are similar for L-MREE, but display large variations in HREE, with patterns varying from positive to negative slope independent of textural position (Figure 12b). A weak to irrelevant Eu anomaly is present. This nonsystematic trace element composition is either due to cut effects (there is no certainty that the two garnet sections cut across the same zones) or reflects original patchy zoning, which is also observed in the Ca distribution (see map of garnet B in Figure 9).

[38] Monazites from gneiss 10–20 have large trace element variations, comparable to garnet, with the highest differences in HREE (from ~20 to 700 chondrite, Figure 12c). However, there is no robust correlation between monazite composition and textural location or age. For example, monazite grains D and O are both ~39 Ma but differ in Lu content by a factor of 10 (Table 4); similarly, monazite grains O and P are both

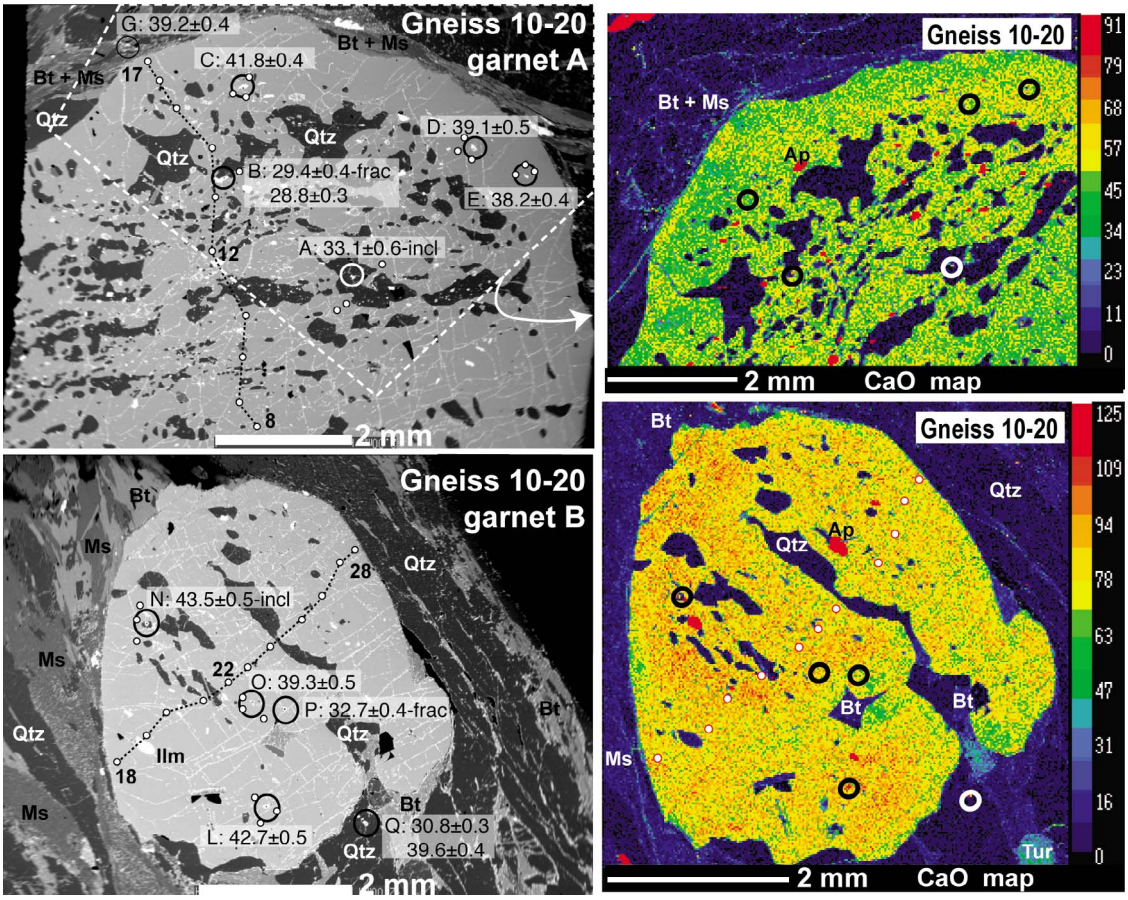

Figure 9. (left) BSE images and (right) CaO maps of two garnet crystals from sample 10–20 with inclusions of dated monazite. Circles, monazite crystals; white dots, LA-ICPMS analyses of trace elements. The dotted line along LA-ICPMS analyses represents the profile presented in Figure 12a. Numbers along this profile indicate the analysis number reported in Figure 12a. For each monazite crystal, label (A, B, etc.) and the $^{206}Pb/^{238}U$ age (Ma ± 1σ) is reported in the BSE image, together with textural comments (incl, monazite included in another mineral in turn included in garnet; frac, monazite lying on a garnet fracture). Mineral abbreviations are according to *Kretz* [1983].

located in the center of the garnet but have different HREE patterns. Nonetheless, the majority of monazite crystals dated at ~39 or 44 Ma have composition strongly depleted in HREE and Y (Figure 12c). The same is observed for the ~39 Ma monazite included in garnet in sample 10–99. Th and Y have been used previously to relate monazite formation to metamorphic evolution [*Foster et al.*, 2000; *Kohn et al.*, 2005]. In our sample, however, Th contents are similar for monazite of all ages and Y can vary within monazite of the same age (Table 4).

[39] The lack of typical bell-shape zoning in garnet or straightforward correlation between monazite age and composition does not hamper the calculation of trace element partitioning between adjacent monazite and garnet. Trace element zoning may resemble the patchy CaO zoning (Figure 9) and thus may be difficult to reconcile with core-rim textures. As a consequence, garnet composition was repeatedly measured (three analyses) in the close proximity of seven of the dated monazites. The partitioning for HREE between monazite and nearby garnet is presented in Figure 12d and shows considerable variation, with $D_{mnz/grt}$ for Lu ranging between 0.3 and 10. The significance of this chemical signature is discussed in detail below.

7. Discussion

7.1. Toijem Shear Zone

[40] The HHC is often regarded as a single tectonic unit, cropping out all over the Himalayan belt with striking continuity and showing mainly variations in the thickness of its formations or units. Recent tectonic models such as channel flow [*Gruijc et al.*, 1996; *Beaumont et al.*, 2001] have further strengthened the relatively simple tectonic and metamorphic evolution of the HHC [*Gruijc*, 2006]. Although described as a large uniform unit, our field work in western Nepal revealed the presence of the TSZ ductile shear zone in the core of the HHC. On the basis of the north dipping of the shear zone and top-to-the-SW sense of shear (Figure 5), we interpret the TSZ as a contractional shear zone that accommodated shortening during the India-Asia convergence. Mylonites

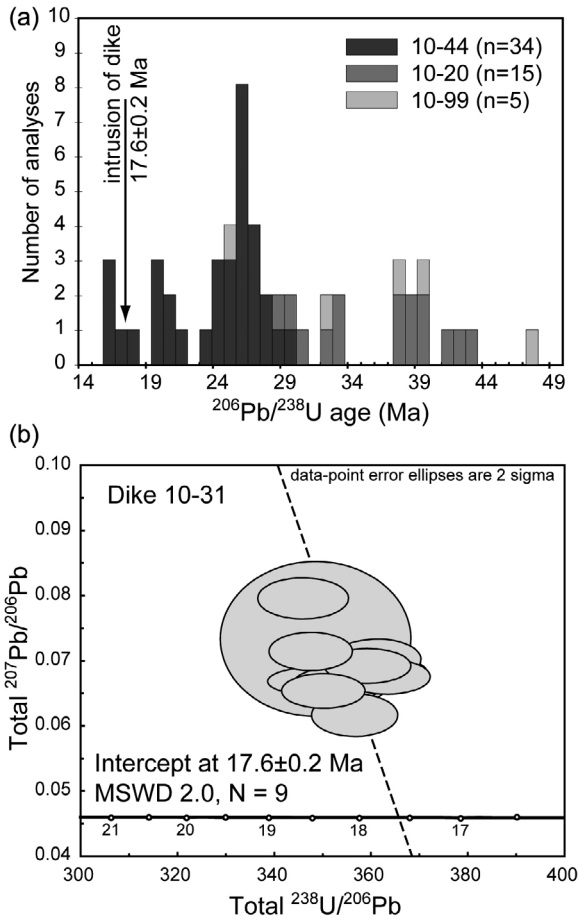

Figure 10. Geochronological results. (a) Histogram of U-Pb ages measured on monazite from three samples. Errors on single ages are between 0.2 and 0.4 Ma (1σ, see Table 3). (b) Tera-Wasserburg plot for uncorrected SHRIMP analyses for dike 10–31. Regression is forced to model of common Pb composition at 17 Myr.

from the TSZ overprint the S_1 foliation and contain sillimanite along the mylonitic foliation, deforming previous kyanite porphyroclasts.

[41] This conclusion matches previous studies [*Lombardo et al.*, 1993; *Pognante and Benna*, 1993; *Hodges et al.*, 1996; *Carosi et al.*, 1999; *Hodges*, 2000, and references therein; *Borghi et al.*, 2003; *Guillot et al.*, 2008] reporting that the HHC underwent, during the Eocene, an HP phase of metamorphism reaching kyanite grade followed by a decompressional phase in the sillimanite stability field during the Oligocene-lower Miocene. In addition, in the nearby Annapurna range, temperature and pressure estimates in micaschists and gneisses confirm an early stage of relatively high pressure conditions, in the kyanite stability field [*Hodges et al.*, 1996; *Vannay and Hodges*, 1996; *Godin et al.*, 2001; *Guillot et al.*, 2008].

[42] Sillimanite-grade metamorphism overprints kyanite-bearing rocks within the HHC and, together with inversion of metamorphism along the MCT zone, constitutes the two examples of inversion of isograds in the Himalayas. Several processes may explain this metamorphic inversion from "hot-iron effect" (emplacement of hot rocks over cold rocks), postmetamorphic thrusting, syn-metamorphic shearing, non-coaxial flow, channel flow, and shear heating as well as decompressional melting associated with leucogranite emplacement during exhumation [*Le Fort*, 1975; *Hubbard*, 1989; *Gruijc et al.*, 1996; *Beaumont et al.*, 2001; *Goscombe et al.*, 2006; *Kohn*, 2008].

[43] To explain this metamorphic inversion within the HHC, a structural discontinuity between the upper sillimanite-grade rocks and the lower kyanite-bearing rocks has been postulated by several authors. *Treloar et al.* [1989] proposed the occurrence of a thrust between sillimanite- and kyanite-bearing rocks in north Pakistan, below the Main Mantle thrust. *Swapp and Hollister* [1991] proposed a cryptic postmetamorphic thrust in the thick sequence of the HHC in the Bhutan Himalayas, predating the MCT. However, *Davidson et al.* [1997] identified this thrust as the out-of-sequence Kakhtang thrust, dated at ~12–14 Ma [*Daniel et al.*, 2003]. A tectonic discontinuity between the two HHC metamorphic zones has been hypothesized in the Langtang section [*Harris and Massey*, 1994; *Macfarlane*, 1995; *Kohn et al.*, 2005], in central Nepal, based on rock textures, isotopic signatures [*Inger and Harris*, 1993; *Reddy et al.*, 1993] and pressure differences larger than lithostatic gradient [*Fraser et al.*, 2000].

[44] We propose that the activity of the TSZ, caused by continuing contraction, enhanced the exhumation of the HHC above the TSZ. As a consequence, the rocks in the hanging wall of the TSZ began to invert their displacement (previously north-downward) and became decompressed (movement south-upward) (Figure 13).

[45] Our estimates indicate different P-T-t paths for the hanging wall and footwall of the TSZ (Figure 8). The movement along the TSZ initiated exhumation of the hanging wall from pressures of 7–7.5 kbar, whereas the footwall continued to be underthrust, reaching pressures of ~9 kbar. This stage was then followed by the overall exhumation of the HHC (Figure 13). Decompression may have triggered melting of high-temperature gneiss, producing the leucogranites found in the hanging wall of the TSZ. This fits the occurrence of melts of 26 Ma as documented by *Viskupic et al.* [2005] in the Khumbu area of the Mt. Everest section and suggests the more extensive occurrence and importance of localized deformation in the tectonic evolution of the HHC.

[46] Because the TSZ started to move during the underthrusting of the HHC, it changed the fate of the TSZ hanging wall rocks that were the first to be exhumed in the HHC: hanging wall rocks inverted their displacement, ceasing to go into depth and starting to move upward and southward. It is worth noting that by activation of the TSZ and before MCT movement, the footwall rocks continued to be buried, reaching higher pressures with respect to hanging wall rocks. As a consequence, the activity of TSZ during underthrusting of HHC produced two different P-T-t paths for footwall and hanging wall rock (Figure 8). If we consider only the P-T-t paths, without the exact deformation path of the rocks considered or, at least, the geometry and kinematic indicators in mylonite, we could erroneously interpret the TSZ to be a normal sense shear zone (in contrast to the movement indi-

Table 3. SHRIMP U, Th-Pb Analyses of Monazite

Label	Position or Zoning	U (wt %)	Th (wt %)	Th/U	% common Pb	Total $^{238}U/^{206}Pb$	±1Sigma	Total $^{207}Pb/^{206}Pb$	±1Sigma	$^{206}Pb/^{238}U$	±1Sigma	$^{206}Pb/^{238}U$ Age	±1Sigma
Gneisses in the Footwall													
1020-B1	in garnet	0.54	3.3	6.1	8.5	204.37	2.15	0.11415	0.00115	0.00448	0.00005	28.8	0.3
1020-B2	in garnet	0.48	2.9	6.0	5.9	205.65	2.14	0.09306	0.00599	0.00458	0.00006	29.4	0.4
1020-Q1	matrix	0.63	3.7	5.8	5.7	196.58	2.00	0.09195	0.00236	0.00480	0.00005	30.8	0.3
1020-B	in garnet	1.70	10	6.1	5.5	190.37	2.35	0.09043	0.00190	0.00496	0.00006	31.9	0.4
1020-P	in garnet	0.69	3.4	5.0	11.7	173.33	1.79	0.13948	0.00131	0.00509	0.00005	32.7	0.4
1020-A	in garnet	1.46	7.0	4.8	1.5	191.16	3.22	0.05893	0.00143	0.00515	0.00009	33.1	0.6
1020-R	matrix	0.41	3.3	7.9	18.1	157.93	1.65	0.19010	0.00135	0.00518	0.00006	33.3	0.4
1020-H	matrix	0.83	4.4	5.3	0.0	173.48	2.96	0.02390	0.01559	0.00593	0.00015	38.1	1.0
1020-E	in garnet	1.05	4.8	4.5	0.6	167.26	1.67	0.05183	0.00044	0.00594	0.00006	38.2	0.4
1020-D	in garnet	1.37	8.8	6.4	0.8	163.04	2.02	0.05312	0.00134	0.00608	0.00008	39.1	0.5
1020-G1	matrix	0.47	3.8	8.0	4.2	157.18	1.67	0.08024	0.00101	0.00609	0.00007	39.2	0.4
1020-0	in garnet	0.55	4.9	8.9	1.2	161.59	1.89	0.05595	0.00155	0.00612	0.00007	39.3	0.5
1020-Q	matrix	0.41	3.8	9.3	0.9	160.73	1.67	0.05395	0.00064	0.00617	0.00006	39.6	0.4
1020-C	in garnet	0.43	4.0	9.3	1.9	150.69	1.56	0.06212	0.00089	0.00651	0.00007	41.8	0.4
1020-L	in garnet	0.39	4.7	11.9	0.6	149.73	1.58	0.05131	0.00066	0.00664	0.00007	42.7	0.5
1020-N	in garnet	0.48	3.3	6.8	0.8	146.32	1.56	0.05346	0.00070	0.00678	0.00007	43.5	0.5
1099-A1	in garnet	0.00	0.0	5.4	1.9	282.02	2.16	0.06185	0.00069	0.00348	0.00003	22.4	0.2
1099-B	matrix	0.92	4.9	6.2	2.6	250.80	1.66	0.06725	0.00076	0.00388	0.00003	25.0	0.2
1099-A2	matrix	0.48	3.0	6.8	1.4	195.23	1.23	0.05802	0.00072	0.00505	0.00003	32.5	0.2
1099-D	matrix	0.65	4.4	7.7	2.1	165.41	1.05	0.06322	0.00050	0.00592	0.00004	38.1	0.2
1099-A	in garnet	0.57	4.4	8.5	0.9	162.38	1.05	0.05397	0.00059	0.00610	0.00004	39.2	0.3
1099-D1	matrix	0.48	4.1	6.4	0.3	134.18	0.94	0.04962	0.00068	0.00743	0.00005	47.7	0.3
1099-D1	matrix	0.53	3.4	6.4	0.3	134.18	0.94	0.04962	0.00068	0.00743	0.00005	47.7	0.3
Mylonite													
1044–13.2	unzoned grain	1.06	n.a	n.a	1.8	383.52	6.03	0.00261	0.00004	0.00256	0.00004	16.5	0.3
1044–29.1	unzoned rim	2.01	n.a	n.a	1.4	383.89	4.12	0.00260	0.00003	0.00257	0.00003	16.5	0.2
1044–35.1	unzoned rim	0.81	n.a	n.a	2.4	376.59	4.15	0.00266	0.00003	0.00259	0.00003	16.7	0.2
1044–19.3	unzoned rim	0.84	n.a	n.a	2.4	359.92	4.18	0.00278	0.00003	0.00271	0.00003	17.5	0.2
1044–1.3	unzoned rim	0.93	n.a	n.a	2.5	341.23	3.68	0.00293	0.00003	0.00286	0.00003	18.4	0.2
1044–10.2	banded core	0.99	n.a	n.a	2.0	319.40	3.62	0.00313	0.00004	0.00307	0.00003	19.8	0.2
1044–34.1	unzoned rim	1.13	n.a	n.a	1.3	320.91	3.40	0.00312	0.00003	0.00308	0.00003	19.8	0.2
1044–6	unzoned grain	1.10	n.a	n.a	1.5	317.13	4.52	0.05853	0.00056	0.00311	0.00004	20.0	0.3
1044–37.1	unzoned grain	1.17	n.a	n.a	1.4	309.91	5.28	0.00323	0.00005	0.00318	0.00005	20.5	0.4
1044–31.1	unzoned grain	0.73	n.a	n.a	2.3	299.18	3.42	0.00334	0.00004	0.00327	0.00004	21.0	0.2
1044–15.2	unzoned rim	1.53	n.a	n.a	1.1	298.11	3.39	0.00335	0.00004	0.00332	0.00004	21.4	0.2
1044–23.2	unzoned rim	0.41	n.a	n.a	2.7	266.68	3.14	0.00375	0.00004	0.00365	0.00004	23.5	0.3
1044–3	unzoned grain	0.87	n.a	n.a	2.2	263.02	3.83	0.06356	0.00065	0.00372	0.00005	23.9	0.4

Table 3. (continued)

Label	Position or Zoning	U (wt %)	Th (wt %)	Th/U	% common Pb	Total $^{238}U/^{206}Pb$	±1Sigma	Total $^{207}Pb/^{206}Pb$	±1Sigma	$^{206}Pb/^{238}U$	±1Sigma	$^{206}Pb/^{238}U$ Age	±1Sigma
1044–12	unzoned grain	0.58	n.a	n.a	2.6	257.37	3.97	0.06731	0.00106	0.00378	0.00006	24.3	0.4
1044–33.1	unzoned rim	0.77	n.a	n.a	0.6	260.40	2.85	0.00384	0.00004	0.00382	0.00004	24.6	0.3
1044–4	banded core	0.68	n.a	n.a	1.7	252.35	3.78	0.05988	0.00073	0.00390	0.00006	25.1	0.4
1044–23.3	patchy core	0.63	n.a	n.a	1.8	251.72	3.07	0.00397	0.00005	0.00390	0.00005	25.1	0.3
1044–10	unzoned core	1.15	n.a	n.a	2.1	249.05	3.45	0.06316	0.00079	0.00393	0.00005	25.3	0.4
1044–2	unzoned grain	0.63	n.a	n.a	3.1	241.61	3.57	0.07074	0.00088	0.00401	0.00006	25.8	0.4
1044–8.3	sector zoning	0.84	n.a	n.a	0.7	246.80	2.72	0.00405	0.00004	0.00402	0.00004	25.9	0.3
1044–21.2	sector zoning	0.83	n.a	n.a	0.4	247.53	5.78	0.00404	0.00009	0.00403	0.00009	25.9	0.6
1044–28.1	unzoned core	0.85	n.a	n.a	0.8	245.79	2.92	0.00407	0.00005	0.00403	0.00005	26.0	0.3
1044–7	unzoned grain	0.57	n.a	n.a	3.4	238.99	3.58	0.07374	0.00116	0.00404	0.00006	26.0	0.4
1044–1	unzoned grain	0.65	n.a	n.a	3.5	238.08	3.53	0.07388	0.00092	0.00405	0.00006	26.1	0.4
1044–30.1	unzoned rim	0.85	n.a	n.a	0.5	244.11	2.69	0.00410	0.00005	0.00408	0.00005	26.2	0.3
1044–36.1	unzoned rim	0.90	n.a	n.a	0.4	242.64	2.69	0.00412	0.00005	0.00411	0.00005	26.4	0.3
1044–32.1	sector zoning	0.65	n.a	n.a	0.9	238.35	2.67	0.00420	0.00005	0.00416	0.00005	26.7	0.3
1044–7.2	unzoned grain	0.59	n.a	n.a	0.7	236.19	5.96	0.00423	0.00011	0.00420	0.00011	27.1	0.7
1044–5	banded core	0.58	n.a	n.a	3.2	230.11	3.26	0.07190	0.00138	0.00421	0.00006	27.1	0.4
1044–11	banded core	0.67	n.a	n.a	3.2	227.61	3.18	0.07167	0.00083	0.00425	0.00006	27.4	0.4
1044–5.4	unzoned grain	0.28	n.a	n.a	2.7	223.24	3.28	0.00448	0.00007	0.00436	0.00006	28.0	0.4
1044–15	banded core	0.77	n.a	n.a	0.5	225.84	3.27	0.05056	0.00059	0.00441	0.00006	28.3	0.4
1044–9.2	dark core	0.89	n.a	n.a	0.5	225.14	3.14	0.05080	0.00081	0.00442	0.00006	28.4	0.4
1044–9.1	unzoned rim	1.01	n.a	n.a	1.1	214.74	3.00	0.05562	0.00069	0.00460	0.00006	29.6	0.4
						Crosscutting Dike							
1031–10	weak oscillatory	2.0	5.4	2.7	2.70	363.34	3.69	0.06775	0.00107	0.00268	0.00003	17.2	0.2
1031–1	weak oscillatory	2.2	8.8	4.0	2.79	361.76	4.05	0.06842	0.00098	0.00269	0.00003	17.3	0.2
1031–7	weak oscillatory	1.5	5.3	3.5	3.04	361.28	3.76	0.07043	0.00126	0.00268	0.00003	17.3	0.2
1031–13	unzoned	2.0	5.9	3.0	2.92	359.38	3.64	0.06943	0.00107	0.00270	0.00003	17.4	0.2
1031–12	weak oscillatory	1.9	7.3	3.8	1.97	356.70	3.63	0.06193	0.00132	0.00275	0.00003	17.7	0.2
1031–8	oscillatory	1.9	7.9	4.2	2.56	353.32	3.85	0.06666	0.00107	0.00276	0.00003	17.8	0.2
1031–3	weak oscillatory	2.2	9.4	4.2	2.62	352.19	5.49	0.06709	0.00099	0.00276	0.00004	17.8	0.3
1031–6	weak oscillatory	1.8	6.9	3.8	4.22	346.09	3.81	0.07973	0.00128	0.00277	0.00003	17.8	0.2
1031–9	unzoned	1.3	6.9	5.5	3.43	348.58	8.04	0.07352	0.00481	0.00277	0.00007	17.8	0.4
1031–4	weak oscillatory	2.1	6.5	3.1	3.20	347.60	3.51	0.07165	0.00119	0.00278	0.00003	17.9	0.2
1031–2	weak oscillatory	1.8	6.8	3.8	2.43	350.21	3.52	0.06562	0.00107	0.00279	0.00003	17.9	0.2

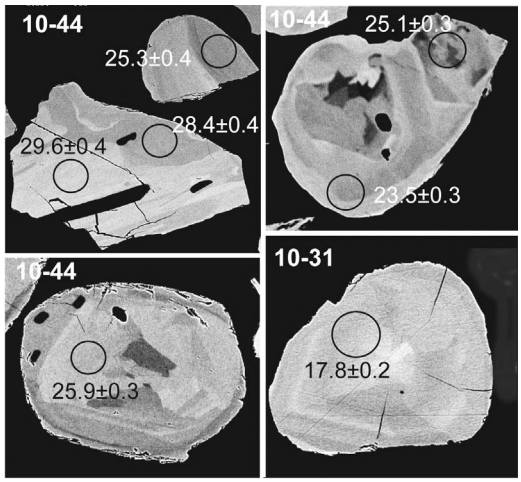

Figure 11. BSE images of dated monazite crystals from mylonite 10–44 and dike 10–31. Circles (~20 μm diameter): location of SHRIMP analyses for which $^{206}Pb/^{238}U$ ages (Ma ± 1σ) are reported.

cated by kinematic indicators in the mylonite) because relatively lower pressure rocks occur in the hanging wall. A main consequence, from this case study, is that interpreting the sense of movement of tectonic structures having only the P-T-t paths may lead to erroneous interpretations.

7.2. Age Interpretation

[47] The monazites in the studied gneiss have ages ranging well above analytical uncertainty. Monazite is resistant to Pb loss by volume diffusion at the temperatures of the samples [*Cherniak et al.*, 2004]. Monazite, unlike zircon, easily recovers from lattice damage and does not become metamict [*Meldrum et al.*, 1998]. This implies that the age range observed is unlikely to be the product of recent Pb loss. We must therefore consider that multiple monazite formation by new growth or recrystallization occurred in the investigated samples. In gneiss 10–99 and 10–20, zoning in monazite was not detected. In mylonite 10–44, monazite zoning, as shown by BSE imaging, is complex; thus, some ages may be the result of the physical mixing of different domains. As a consequence, this discussion focuses on the main age clusters, disregarding isolated ages.

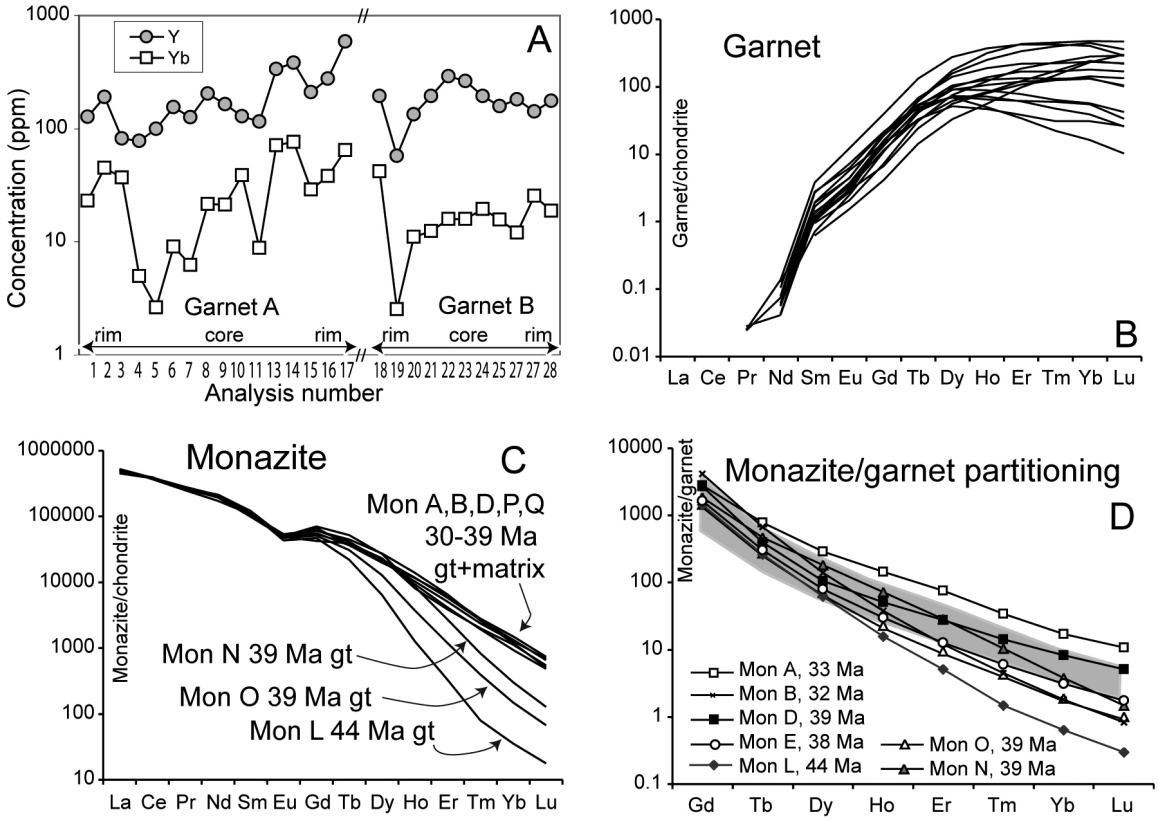

Figure 12. Trace element composition of garnet and monazite from gneiss sample 10–20. (a) Y and Yb profiles across two distinct garnet crystals. (b) Chondrite−normalized garnet patterns. There is no straightforward correlation between composition and textural position. See Table 4 for representative analyses. (c) Chondrite−normalized REE patterns of dated monazites. Data from Table 4. (d) Calculated REE partitioning between monazites of various ages included in garnet and the adjacent garnet. Shaded band: range of equilibrium partitioning, according to *Hermann and Rubatto* [2003], *Buick et al.* [2006], and *Rubatto et al.* [2006]. See text for discussion.

Table 4. LA-ICPMS Analyses of Garnet (Representative Analyses Used for Partitioning Calculation) and Monazite[a]

	1020-A	1020-B	1020-D	1020-E	1020-C	1020-O	1020-N	1020-L	1020-S
					Garnet				
P	187	134	245	283	253	98	146	211	115
Ti	46	39	44	51	42	42	43	42	42
Rb	<0.05	0.12	0.07	0.09	0.11	0.06	0.06	<0.05	2.00
Sr	0.01	0.07	0.02	0.04	0.03	0.01	0.01	<0.008	0.09
Y	140	315	317	437	369	205	135	105	338
Zr	2.6	2.0	3.1	4.1	3.3	2.4	2.8	3.3	2.0
La	<0.005	0.013	<0.005	0.025	0.038	<0.005	0.008	0.015	0.021
Ce	0.003	<0.001	0.007	0.031	0.030	0.008	0.006	0.050	0.051
Pr	0.004	<0.001	<0.001	0.005	0.008	<0.001	0.005	0.005	0.010
Nd	0.039	0.047	0.036	0.055	0.049	0.037	0.037	0.066	0.087
Sm	0.27	0.11	0.25	0.40	0.24	0.25	0.33	0.31	0.22
Eu	0.26	0.13	0.24	0.36	0.24	0.28	0.32	0.30	0.24
Gd	3.8	2.2	4.1	5.7	4.4	6.6	6.2	5.7	5.6
Tb	1.8	1.7	2.7	3.7	2.9	3.8	3.2	2.6	3.8
Dy	20	34	39	53	44	42	30	23	53
Ho	4.4	14	10	16	14	8.3	5.3	3.9	13
Er	12	65	30	53	47	19	13	9	38
Tm	1.6	12.5	4.0	8.2	7.0	2.2	1.6	1.2	5.0
Yb	10	101	24	55	48	12	10	8.0	31
Lu	1.0	16.7	3.0	8.2	7.0	1.5	1.7	1.3	4.4
Hf	0.054	0.045	0.057	0.060	0.047	0.035	0.064	0.039	0.059
Pb	0.027	0.036	0.024	0.038	0.028	0.026	0.021	0.022	0.031
Th	<0.002	<0.002	0.006	<0.002	<0.002	<0.002	<0.002	0.009	0.087
U	<0.002	0.030	<0.002	0.020	0.010	<0.002	0.009	0.008	0.021
Lu/Gd*	2.1	60.6	5.9	11.6	12.7	1.9	2.3	1.8	6.4
	1020-A	1020-B	1020-D	1020-E	1020-O	1020-N	1020-L	1020-P	1020-Q
					Monazite				
Position	Grt core	Grt core	Grt rim	Grt rim	Grt core	Grt rim	Grt mantle	Grt core	Matrix
Age (Ma)	33.1	31.9	39.1	38.2	39.3	43.6	42.7	32.7	39.6
Ti	n.a	4.4	6.1	5.8	6.7	3.8	4.6	4.2	5.0
Y	17,505	15,054	12,444	13242	5138	11767	1688	12498	14023
Zr	2.4	1.4	1.2	1.5	1.1	1.5	1.0	1.2	1.7
Nb	n.a	0.07	0.06	0.07	0.11	0.08	0.07	0.08	0.08
La	113,233	119,837	106,722	118,814	124,001	121,893	124,334	123,866	123,273
Ce	240,682	234,137	23,5469	232,272	236,146	236,146	237,400	228,123	237,213
Pr	24,590	25,511	24,987	25,274	25,610	25,955	25,511	23,377	25,958
Nd	89,225	91,613	98,145	91,248	94,972	96,413	90,754	79,020	95,921
Sm	14,544	16,094	18,009	16,114	16,879	17,270	16,748	15,966	16,028
Eu	2747	2769	2799	2647	2645	2826	2448	2733	3035
Gd	12,122	10,839	13,373	11,154	10,238	14,060	9330	8456	12,313
Tb	1616	1368	1316	1331	1111	1871	793	1412	1486
Dy	6697	5557	4899	5084	3167	6584	1592	5686	5371
Ho	765	641	630	560	203	469	70	448	509
Er	1048	927	988	807	192	437	53	619	666
Tm	65	66	69	59	10	21	2	50	48
Yb	192	215	242	205	24	49	6	183	152
Lu	13	16	18	17	1.7	3.1	0.43	13	12
Hf	0.26	0.23	0.16	0.19	0.07	0.26	<0.005	0.21	0.24
Ta	n.a.	0.04	0.07	0.06	0.03	0.07	0.02	0.06	0.04
Th	51,144	47,543	48,791	49,200	45,163	46,633	46,881	36,825	55,250
U	6366	5875	5333	8259	5007	7111	6764	7371	9306
Gd/Lu*	117	82	88	80	752	546	2604	76	125

[a]Values in ppm.

7.2.1. Monazite in the Footwall of the Toijem Shear Zone

[48] In gneiss 10–20 and 10–99, age variations do not necessarily correspond to textural positions; for example, monazites included in the core of the garnet are younger than grains included in garnet rims (Figure 9). Some monazite grains in garnet lie along fractures or at the border of biotite inclusions, meaning that secondary monazite inclusions or infiltration of fluids along fractures may have caused monazite recrystallization. Thus, caution must be exercised when using textural relationships for monazite age interpretation. However, some broad criteria are appropriate. The oldest monazite was found exclusively as an inclusion in garnet in sample 10–20 (Figure 9), within the Ca-rich domains. Some

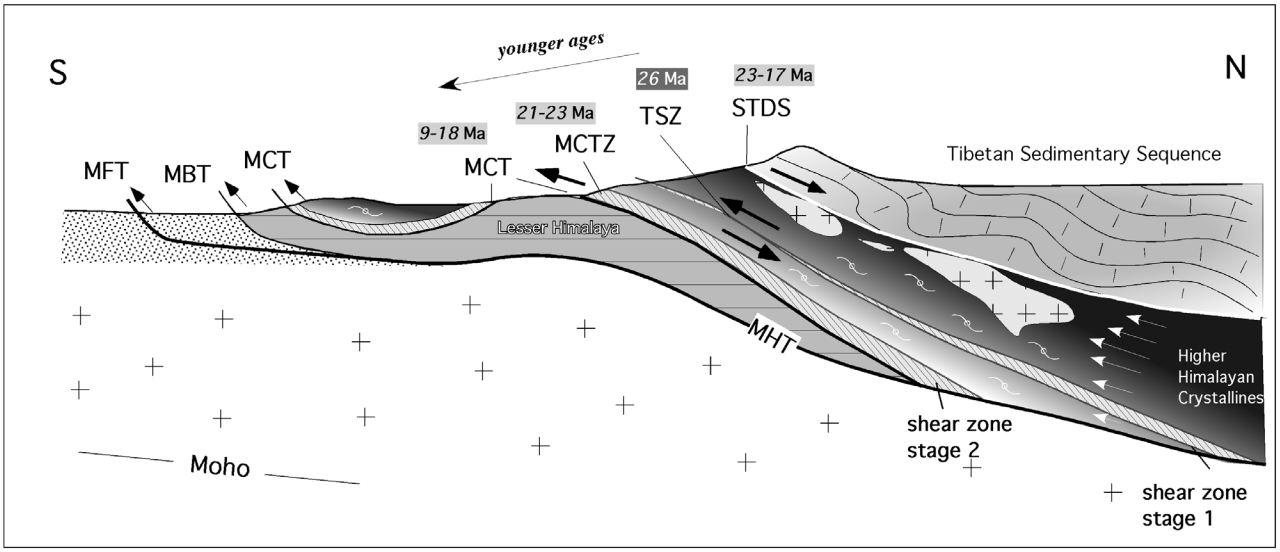

Figure 13. Schematic cross section throughout the Himalayas showing the main tectonic structures and their ages. Ages of ductile shear zones such as TSZ and MCTZ and subsequent brittle faults in western Nepal indicate a deformation propagating to the foreland. Ages of STDS and MCT in central−western Nepal are from review by *Godin et al.* [2006]. Cross section redrawn from *Bollinger et al.* [2006]. Abbreviations as in Figure 2. MCTZ, Main Central Thrust Zone; TSZ,Toijem shear zone; MBT, Main Boundary Thrust; MFT, Main Frontal Thrust; MHT, Main Himalayan Thrust. Crosses with gray background indicate Higher Himalayan granites emplaced in the hanging wall of the TSZ.

of these monazites have the lowest Y content measured (Figure 12c). This suggests that the 43-Ma-old monazite formed during an early stage of garnet growth, which sequestrated Y.

[49] The main monazite population, dated at 39.0 ± 0.6 Ma, occurs in garnet and matrix. Some of the 39-Ma-old grains are fully enclosed in garnet rims without any evidence of fracturing (grains D and E in Figure 9). Zoning in inclusions, CaO, and trace elements in garnet is complex and supports the existence of distinct growth stages, which would then be reflected in monazite growth at ~43 and 39 Ma. These observations and trace element partitioning (Figure 12d) suggest that the 39-Ma-old monazite grains are primary inclusions and were included in the garnet rim at growth. Of the apparent partitioning calculated between adjacent monazite-garnet pairs, those for 39-Ma-old monazites (grains D, E, and O) are in the previously published range of equilibrium HREE partitioning [*Hermann and Rubatto*, 2003; *Buick et al.*, 2006; *Rubatto et al.*, 2006]. Such monazites vary from low- to high-Y content with respect to the rest of the population (Figure 12c) and may indicate that some early garnet was dissolved during the growth of 39 Ma monazite to provide for Y. Trace element disequilibrium, as indicated by erroneous partitioning (Figure 12d), is observed between some monazites and the surrounding garnet. This may be explained by the formation of monazite by fluids infiltrating the garnet along fractures, or inclusions in the garnet of relict monazite (see also *Kohn et al.* [2005]).

[50] Monazites yielding a ~33 Ma age were found both inside and outside the garnet. However, the four grains included in garnet lie near fractures in low-Ca domains, or within inclusions of quartz and biotite (Figure 9). These monazites are rich in HREE and Y (Figure 12c), as expected if some garnet dissolution occurred before or during the growth of 33-Ma-old monazite. Garnet resorption is supported by the rounded shape of the garnet crystals (Figure 9). We propose that such monazites represent secondary inclusions, or have been exposed to the action of metamorphic fluids. We tentatively suggest that monazite dated at 33 Ma or younger formed or recrystallized after the garnet growth.

7.2.2. Monazite in the Toijem Shear Zone

[51] Monazite in mylonite sample 10–44 occurs in the matrix and as inclusions in garnet. In this sample, monazite was dated as mineral separate, and separation may have failed to recover all or some of the monazite grains included in garnet, and the older evolution of the sample may have been missed in part. Even assuming a bias toward younger ages, it is evident that this sample records a younger history than samples 10–20 and 10–99 (Figure 11): only a few ages from sample 10–44 are as old as ~28 Ma, the youngest age measured in sample 10–20. The main age population at 25.8 ± 0.3 Ma is not represented in sample 10–20, whereas a single monazite of this age was found in the matrix of sample 10–99. None of the younger ages measured in sample 10–44 were detected in the kyanite-bearing gneiss.

[52] The major difference between mylonite 10–44 and the kyanite-bearing gneiss is the main sillimanite-bearing foliation, which is wrapped around kyanite relicts, indicating that higher pressure conditions (kyanite-bearing), similar to those recorded in the gneiss, were achieved before mylonitization.

Thus, the main monazite population (25.8 ± 0.3 Ma) found in the mylonite formed together with the sillimanite-bearing foliation. This agrees with the ~25-Ma-old monazite dated in sample 10–99, in which sillimanite also occurs. Older ages at ~28 Ma would then be related to the metamorphic history of the mineral relicts in the kyanite stability field. Monazites younger than ~26 Ma are interpreted as forming or recrystallizing during later deformation along the shear zone.

[53] Leucogranite sample 10–31 has one main monazite population with oscillatory zoning, suggesting a magmatic origin [*Pidgeon*, 1992]. The monazite age is therefore interpreted as dating the emplacement of the dike at 17.6 ± 0.2 Ma. The weak deformation within the dike is thus interpreted as the final activity of the shear zone that the dike cuts.

[54] The end of the main deformation in the HHC at ~17 Ma is in keeping with the analysis of sediment composition and detrital mica age in the Himalayan foreland by *White et al.* [2002], *Garzanti et al.* [2007], and *Najman et al.* [2008] and with the absence of younger ductile fabrics [*Searle and Godin*, 2003; *Carosi et al.*, 2006].

[55] In conclusion, monazite dating in samples adjacent to and within the TSZ indicates that the activity of this shear zone within the HHC peaked at 25.8 ± 0.3 Ma and probably continued until 17.6 ± 0.2 Ma. Monazites in the gneisses of the footwall of the TSZ point to high-pressure metamorphism in the kyanite stability field at ~43 Ma that possibly lasted until ~33 Ma.

7.3. Tectonics Within the HHC and Exhumation

[56] Ductile to brittle shear zones have been identified within the HHC in other areas of the belt, e.g., the Annapurna Range (Kalopani shear zone [*Vannay and Hodges*, 1996] and Modi Khola shear zone [*Hodges et al.*, 1996]), in Langtang [*Macfarlane*, 1993; *Kohn et al.*, 2005], in the Mt. Everest region (Khumbu Thrust [*Maruo and Kizaki*, 1983; *Searle*, 1999]), in the Arun Valley (Barun thrust [*Goscombe and Hand*, 2000]), and in Bhutan (Kakhtang thrust [*Grujic et al.*, 1996; *Davidson et al.*, 1997]). They are often regarded as syn- to postmetamorphic out-of-sequence thrusts, sometimes doubling the HHC sequence (e.g., Kakhtang thrust). Their ages are constrained at ~22.5–18.5 Ma in central Nepal [*Hodges et al.*, 1996] and ~15–13 Ma in central Nepal and Bhutan [*Vannay and Hodges*, 1996; *Grujic et al.*, 2002; *Khon et al.*, 2005]. Recently, normal-sense shear zones have been described in the middle portion of the HHC in Bhutan [*Carosi et al.*, 2006]. The Bhutan shear zone is dated at ~20–17 Ma and related to the lengthening of the core of the HHC in response to the pure shear component of noncoaxial deformation during extrusion.

[57] *Goscombe et al.* [2006] described a high-strain zone at high structural levels in the HHC in the Mt. Makalu and Mt. Kanchenjunga areas, well above the MCT. This strain zone was called the High Himalaya thrust and is a first-order structure controlling the architecture of the belt and marking a steep metamorphic transition. The High Himalaya thrust has been tentatively correlated with the upper portion of the MCT zone to the west and with the Kakhtang thrust in eastern Nepal, Sikkim, and Bhutan [*Goscombe et al.*, 2006], although the different ages of the correlated structures represent a problem. There are some similarities between these structures and the high-grade TSZ described here, but the age of the TSZ is older than the High Himalaya thrust and the MCT.

[58] The activity of the TSZ, peaking at ~26 Ma and terminating at ~17 Ma, is older than the main deformation dated in the Langtang-Darondi region to the east, where detailed monazite geochronology exists [*Kohn et al.*, 2005, *Kohn*, 2008]. Movement along the Langtang Thrust [*Reddy et al.*, 1993], at the northern end of the HHC, has been constrained to 21 ± 2 Ma, whereas the MCT, at the southern limit of the HHC, records syn-metamorphic monazite growth at 16 ± 1 Ma [*Kohn*, 2008].

[59] With available geochronological data, it is concluded that the TSZ is one of the oldest contractional shear zones identified until now within the HHC. The location of the TSZ between units 1 and 2 of the HHC suggests that this boundary acted as a zone of weakness. This localized deformation caused the change in the displacement direction of the hanging wall, and recorded the oldest stage of exhumation of the HHC.

[60] Admitting a 40° dip of the TSZ (close to the actual dipping value of the shear planes) and the difference of 2 kbar between two points now in close contact but located in the hanging wall and footwall, respectively, 8 km of horizontal displacement are needed to restore the pre-TSZ position. The original dip angle of the main foliation of the HHC and of the TSZ was probably less than 40° (see, e.g., the overall flat geometry of the HHC required by the channel flow model [*Beaumont et al.*, 2001; *Godin et al.*, 2006]). Decrease in dip of the angle would result in increased horizontal displacement (for a 10° dipping, the displacement would be ~35 km). Taking into account the 5° of hinterland dipping proposed by *Robinson et al.* [2006], the displacement of the TSZ reaches ~70 km. Even these rough estimates clearly indicate the presence of a first-order tectonic structure. The finding of shear zones and exhumation active since ~26 Ma is in agreement with the conclusions obtained by *Garzanti et al.* [2007] and *Najman et al.* [2008], suggesting that exhumation of the HHC started before the MCT's activity (since 38 Myr).

[61] Several exhumation mechanisms for the rocks of the Himalayas have been proposed to date. Thrust propagation to the foreland [*DeCelles et al.*, 2001; *Robinson et al.*, 2003, 2006] and critical taper [*Kohn*, 2008] have also been suggested. Foreland thrust propagation and duplexing have been documented in central and western Nepal in the last 22–20 Ma [*Robinson et al.*, 2003, 2006; *Bollinger et al.*, 2006; *Wobus et al.*, 2006], but although these authors explain deformation at upper crustal level (where rocks undergo the Mohr-Coulomb criterion of fracture), they fail to take into account deformation in the ductile field and Himalayan metamorphism in the HHC.

[62] *Kohn* [2008] made a further effort to include ductile deformation and metamorphism proposing an interesting critical taper model capable of better explaining P-T-t paths for rocks of the HHC with respect to the channel flow model. He applied the critical taper proposed by *Dahlen* [1990] for frictional orogenic wedges. Critical taper mechanics is based on the brittle mechanism of fractures and it can explain the behavior of the external wedge-shaped portion of the orogens. However, a frictional orogenic wedge cannot account

easily for the evolution of ductile and metamorphosed crystalline units because deformation mechanisms in the ductile field change from frictional to plastic. Moreover, the amphibolite and granulite facies meamorphism experienced by the HHC [*Lombardo et al.*, 1993; *Carosi et al.*, 1999; *Guillot et al.*, 1999, with references therein] cannot be achieved by only the lithostatic pressure of the overlying tectonic units in a thrust propagation to the foreland.

[63] The mechanism of exhumation by channel flow or channel flow and extrusion has been proposed by several authors in the Himalayan belt from Bhutan, to Sikkim, to the Mt. Everest area up to central-eastern Nepal [*Gruijic et al.* 2002; *Beaumont et al.* 2001; *Godin et al.* 2006; *Hodges*, 2006]. However, its continuation to the western sector of the belt has been questioned recently by *Leech* [2008], who proposed that the Karakoram fault (terminating just to the northwest of the Nepal-India boundary), which has been active since 25–21 Myr, created a barrier to the southward flow of midcrustal melts. In addition to this, we point out two additional main problems in applying the channel flow model to the study area: (1) in the Dolpo region the thickness of the HHC reaches only 2–4 km, an order of magnitude below the requested thickness (20–30 km) to activate a midcrustal flow [*Gruijic*, 2006; *Godin et al.*, 2006]; (2) the exhumation of the HHC had already started at ~26 Myr with the activity of the ductile Toijem shear zone in the core of the HHC. This is in a different position and some My before the activation of the STDS and MCT (~23–17 Ma) in central-western Nepal (see review of ages of MCT and STDS in *Godin et al.* [2006]). Exhumation starting at 26 Myr is in line with the ~25 Ma Ar/Ar age for muscovite in gneiss in the hanging wall of the MCT in the HHC klippe SW of the study area [*Robinson et al.*, 2006].

[64] Our findings support a model in which, after the main stages of deformation and metamorphism in the HHC (~44 and 33 Myr), deformation propagates from the core of the HHC toward the foreland. Deformation propagates by progressive activation of ductile shear zones at depth beginning 26 Myr, i.e., some My before shearing of the MCT in western Nepal. This was followed by thrusts at higher structural levels. Our results are in line with progressive propagation of deformation toward the foreland, starting from ductile deformation at lower structural levels by activation of TSZ and subsequently of the MCT zone. Deformation and exhumation continued up to upper crustal levels where crystalline rocks and mylonites underwent brittle deformation by thrusts, affecting the MCT zone [*Carosi et al.*, 2007] and propagating to the foreland. This is in agreement with the results that, once the MCT was activated, in the time span between 22 and 20 Myr and the present, progressive thrust activation toward the foreland occurred in western Nepal [*DeCelles et al.*, 2001; *Robinson et al.*, 2003, 2006; *Bollinger et al.*, 2006].

8. Conclusions

[65] Field, structural, petrographic, and geochronological data from the HHC in western Nepal allow reconstruction of the evolution of the Toijem shear zone and its implications for Himalayan tectonics. The TSZ is one of the oldest shear zones within the HHC, being active between ~26 and ~17 Myr. The TSZ caused earlier decompression of the hanging wall, whereas its footwall continued to be underthrust, reaching higher pressure conditions, at least until the activation of the MCT. Geobarometry points to a minimum difference of 2 kbar between hanging wall and footwall, which is the relatively lower pressure reached in the hanging wall even in the presence of a contractional shear zone. This suggests great caution when tectonic structures and their displacement are derived only by differences in metamorphic conditions and the primary role of strain and kinematic indicators in characterizing tectonic structures.

[66] Early monazite growth in the kyanite-bearing gneiss from the lower part of the HHC, now the footwall of the TSZ, constrains collisional deformation and metamorphism between ~43 and 33 Myr. This shear zone marks progressive deformation from hinterland to foreland of the thrust belt. This implies that the TSZ is an important tectonometamorphic discontinuity within the HHC, which was active after the initial collision and mostly before the development of major structures such as the MCT and STDS. The TSZ coincides with the boundary between units 1 and 2 of the HHC. This major lithological discontinuity probably played a crucial role in the localization of deformation in the TSZ.

[67] The activity of the TSZ in the core of the HHC and the subsequent activation of a thick shear zone along its base in the MCT zone, crosscut by further brittle thrusts, indicate a mechanism of progressive propagation of deformation toward the more external areas of the belt in western Nepal.

[68] Both the highly reduced thickness of the HHC and its earlier exhumation by the TSZ point to a mechanism of exhumation that is not compatible with a southern flow of midcrustal melts. As a consequence, a unique mechanism of exhumation of the HHC does not exist over the entire length of the belt, but there is a marked change starting from western Nepal.

Appendix A: Analytical Conditions Used for PT Estimates

[69] Mineral analyses were carried out on WDS CAMECA/CAMEBAX and WDS CAMECA SX 50 electron microprobes. The CAMECA/CAMEBAX operated at 15 kV and 15 nA, with an integration time of 5 s for major elements; natural (Si, Ca, Mg, Al, Na, and K) and synthetic pure (Cr, Fe, Mn, and Ti) oxides were used as standards for calibration. A PAP (CAMECA copyright) program was used to convert counts into weight percents of oxides. Results are considered accurate to within ±2% for major elements and to within ±5% for minor elements. Samples were chosen according to the textural equilibrium among phases of interest and the absence of retrogression.

Appendix B: Methods Used for Monazite Geochronology

[70] Monazite samples were prepared either as mineral separates mounted in epoxy and polished down to expose the grain centers (sample 10–44) or as polished thin sections (samples 10–20, 10–99). The same epoxy or thin-section

samples were used for imaging SHRIMP U-Pb and LA-ICPMS trace element analysis.

[71] The major element composition of garnet and monazite was determined at the Research School of Earth Sciences (RSES, Canberra) on a Cameca SX100 and a Cameca SX50 electron microprobe, respectively. Operating conditions for both machines were 15 kV and 40 nA. Backscattered electron images of monazite were carried out at the Electron Microscope Unit, Australian National University, on a Cambridge S360 scanning electron microscope, voltage of 20 kV, current of ~3 nA, and a working distance of ~20 mm.

[72] Trace element analyses were performed by laser ablation – ICP-MS at the RSES, with a pulsed 193 nm ArF Excimer laser with 100 or 70 mJ energy at a repetition rate of 5 Hz [*Eggins et al.*, 1998] coupled to an Agilent 7500 quadrupole ICP-MS. During the time-resolved analysis of minerals, the contamination from inclusions, fractures, and zones of varying compositions was detected by monitoring several elements and integrating only the relevant part of the signal. Spot sizes of 19 μm for monazite and 70 μm for garnet were used. External calibration was performed relative to NIST 612 glass, at the concentrations given in *Pearce et al.* [1997]. Internal standards were Ca and Si for garnet and Ca and Ce for monazite, as measured by electron microprobe.

[73] U-Th-Pb analyses were performed on a sensitive, high-resolution ion microprobe (SHRIMP II and SHRIMP RG) at the RSES. Instrumental conditions and data acquisition were generally as described by *Williams* [1998]. Data were collected in sets of six or seven scans throughout the masses. The measured $^{206}Pb/^{238}U$ ratio was corrected with reference monazite from the Thompson Mine (TM = 1766 Ma) and Delaware (44069 = 425 Ma) [*Aleinikoff et al.*, 2007]. No energy filtering was applied to suppress the interference on ^{204}Pb, because the data were corrected for common Pb on the basis of the measured $^{207}Pb/^{206}Pb$ ratios as described in *Williams* [1998]. The common Pb composition was assumed to be that of the model Pb evolution for the appropriate age. No correlation was observed between apparent U-Pb age and Th/U or $^{208}Pb/^{206}Pb$, excluding the presence of excess ^{206}Pb from ^{230}Th decay. In addition, when measured (sample 10–44) Th/Pb ages match U/Pb ages. Age was calculated with the Isoplot/Ex software [*Ludwig*, 2000]. Mean ages are at a 95% confidence level; single analyses in both text and tables are reported with an error level of 1σ errors.

[74] **Acknowledgments.** This research was funded by the University of Pisa (R.C., C.M.), PRIN Cofin 2006. D.R. would like to thank the Electron Microscopy Unit at the Australian National University for access to SEM. We are grateful to E. Garzanti for a critical revision of the manuscript. We thank D. Nannini (DST, Pisa) for redrawing the topography for Figure 5. Two anonymous referees are kindly thanked for improving an earlier version of the manuscript.

References

Aleinikoff, J. N., W. S. Schenck, M. O. Plank, L. Srogi, C. M. Fanning, S. L. Kamo, and B. Howell (2007), Deciphering igneous and metamorphic events in high-grade rocks of the Wilmington Complex, Delaware: Morphology, cathodoluminescence and backscattered electron zoning, and SHRIMP U-Pb geochronology of zircon and monazite, *Geol. Soc. Am. Bull.*, *118*, 39–64, doi:10.1130/B25659.1.

Beaumont, C., R. A. Jamieson, M. H. Nguyen, and B. Lee (2001), Himalayan tectonics explained by extrusion of a low-viscosity crustal channel coupled to focused surface denudation, *Nature*, *414*, 738–742, doi:10.1038/414738a.

Beyssac, O., L. Bollinger, J. P. Avouac, and B. Goffé (2004), Thermal metamorphism in the lesser Himalaya of Nepal determined from Raman spectroscopy of carbonaceous material, *Earth Planet. Sci. Lett.*, *225*, 233–241, doi:10.1016/j.epsl.2004.05.023.

Bhattacharya, A., L. Mohanty, A. Maji, S. Sen, and M. Raith (1992), Non-ideal mixing in the phlogopite-annite binary: Constraints from experimental data on Mg-Fe partitioning and a reformulation of the biotite-garnet geothermometer, 111, *Contrib. Mineral. Petrol.*, 87–93, doi:10.1007/BF00296580.

Bollinger, L., P. Henry, and J. P. Avouac (2006), Mountain building in the Nepal Himalaya: Thermal and kinematic model, *Earth Planet. Sci. Lett.*, *244*, 58–71, doi:10.1016/j.epsl.2006.01.045.

Borghi, A., D. Castelli, B. Lombardo, and D. Visona (2003), Thermal and baric evolution of garnet granulites from the Kharta region of S Tibet, E Himalaya, *Eur. J. Mineral.*, *15*(2), 401–418, doi:10.1127/0935-1221/2003/0015-0401.

Brown, R. L., and J. H. Nazarchuk (1993), Annapurna detachment fault in the Greater Himalaya of central Nepal, in *Himalayan Tectonics*, edited by P. J. Treloar and M. P. Searle, *Geol. Soc. Spec. Publ.*, *74*, 461–473.

Buick, I. S., J. Hermann, I. S. Williams, R. Gibson, and D. Rubatto (2006), A SHRIMP U-Pb and LA-ICP-MS trace element study of the petrogenesis of garnet-cordierite-orthoamphibole gneisses from the Central Zone of the Limpopo Belt, South Africa, *Lithos*, *88*, 150–172, doi:10.1016/j.lithos.2005.09.001.

Burchfiel, B. C., and L. H. Royden (1985), North-south extension within the convergent Himalayan region, *Geology*, *13*, 679–682, doi:10.1130/0091-7613(1985)13<679:NEWTCH>2.0.CO;2.

Burchfiel, B. C., Z. Chen, K. V. Hodges, Y. Liu, L. H. Royden, D. Changrong, and L. Xu (1992), The South Tibetan Detachment System, Himalayan Orogen: Extension contemporaneous with and parallel to shortening in a collisional mountain belt, *Spec. Pap. Geol. Soc. Am.*, *269*, 41 pp.

Burg, J. P., M. Brunel, D. Gapais, G. M. Chen, and G. H. Liu (1984), Deformation of leucogranites of the crystalline main central thrust sheet in southern Tibet (China), *J. Struct. Geol.*, *6*, 535–542, doi:10.1016/0191-8141(84)90063-4.

Caby, R., A. Pêcher, and P. Le Fort (1983), Le grand chevauchement central himalayen: Nouvelles données sur le métamorphisme inverse à la base de la Dalle du Tibet, *Rev. Geol. Dyn. Géogr. Phys.*, *24*, 89–100.

Carosi, R., B. Lombardo, G. Molli, G. Musumeci, and P. C. Pertusati (1998), The South Tibetan Detachment System in the Rongbuk valley, Everest region: Deformation features and geological implications, *J. Asian Earth Sci.*, *16*, 299–311, doi:10.1016/S0743-9547(98)00014-2.

Carosi, R., B. Lombardo, G. Musumeci, and P. C. Pertusati (1999), Geology of the Higher Himalayan Crystallines in Khumbu Himal (eastern Nepal), *J. Asian Earth Sci.*, *17*, 785–803, doi:10.1016/S1367-9120(99)00014-0.

Carosi, R., C. Montomoli, and D. Visonà (2002), Is there any detachment in the Lower Dolpo (western Nepal)?, *C. R. Geosci.*, *334*, 933–940, doi:10.1016/S1631-0713(02)01828-X.

Carosi, R., C. Montomoli, and D. Visonà (2006), Normal-sense shear zones in the core of Higher Himalayan Crystallines (Bhutan Himalaya): Evidence for extrusion?, in *Channel Flow, Ductile Extrusion and Exhumation in Continental Collision Zones*, edited by R. D. Law, M. P. Searle, and L. Godin, *Geol. Soc. Spec. Publ.*, *268*, 425–444.

Carosi, R., C. Montomoli, and D. Visonà (2007), A structural transect in the Lower Dolpo: Insights on the tectonic evolution of Western Nepal, *J. Asian Earth Sci.*, *29*, 407–423, doi:10.1016/j.jseaes.2006.05.001.

Catlos, E. J., T. M. Harrison, C. E. Manning, M. Grove, S. M. Rai, M. S. Hubbard, and B. N. Upreti (2002), Records of the evolution of the Himalayan orogen from in situ Th-Pb ion microprobe dating of monazite: Eastern Nepal and western Garhwal, *J. Asian Earth Sci.*, *20*(5), 459–479, doi:10.1016/S1367-9120(01)00039-6.

Catlos, E. J., C. S. Dubey, T. M. Harrison, and M. A. Edwards (2004), Late Miocene movement within the Himalayan Main Central Thrust shear zone, Sikkim, north-east India, *J. Metamorph. Geol.*, *22*, 207–226, doi:10.1111/j.1525-1314.2004.00509.x.

Chemenda, A. I., M. Mattauer, M. Malavieille, and A. N. Bokun (1995), A mechanism for syn-Collisional deep rock exhumation and associated normal faulting: Results from physical modeling, *Earth Planet. Sci. Lett.*, *132*, 225–232, doi:10.1016/0012-821X(95)00042-B.

Cherniak, D. J., E. B. Watson, M. Grove, and T. M. Harrison (2004), Pb diffusion in monazite: A combined RBS/SIMS study, *Geochim. Cosmochim. Acta*, *68*, 829–840, doi:10.1016/j.gca.2003.07.012.

Coleman, M. E. (1996), Orogen-parallel and orogen-perpendicular extension in the central Nepalese Himalayas, *Geol. Soc. Am. Bull.*, *108*, 1594–1607, doi:10.1130/0016-7606(1996)108<1594:OPAOPE>2.3.CO;2.

Crouzet, C., I. Dunkl, L. Paudel, P. Arkai, T. M. Rainer, K. Balogh, and E. Appel (2007), Temperature and age constraints on the metamorphism of the Tethyan Himalaya in central Nepal: A multidisciplinary approach, *J. Asian Earth Sci.*, *30*, 113–130, doi:10.1016/j.jseaes.2006.07.014.

Dahlen, F. A. (1990), Critical taper model of fold-and-thrust belts and accretionary wedges, *Annu. Rev.*

Earth Planet. Sci., *18*, 55–59, doi:10.1146/annurev.ea.18.050190.000415.

Daniel, C. G., L. S. Hollister, R. R. Parrish, and D. Grujic (2003), Exhumation of the Main Central Thrust from lower crustal depths, eastern Bhutan Himalaya, *J. Metamorph. Geol.*, *21*, 317–334.

Davidson, C., D. Grujic, L. S. Hollister, and S. M. Schmid (1997), Metamorphic reactions related to decompression and synkinematic intrusion of leucogranite, High Himalayan Crystallines, Bhutan, *J. Metamorph. Geol.*, *15*, 593–612, doi:10.1111/j.1525-1314.1997.00044.x.

DeCelles, P. G., G. E. Gehrels, J. Quade, T. P. Ojha, P. A. Kapp, and B. N. Upreti (1998), Neogene foreland deposits, erosional unroofing, and the kinematic history of the Himalayan fold-thrust belt, western Nepal, *Geol. Soc. Am. Bull.*, *110*, 2–21, doi:10.1130/0016-7606(1998)110<0002:NFBDEU>2.3.CO;2.

DeCelles, P. G., D. M. Robinson, J. Quade, T. P. Ojha, C. N. Garzione, P. Copeland, and B. N. Upreti (2001), Stratigraphy, structure, and tectonic evolution of the Himalayan fold-thrust belt in western Nepal, *Tectonics*, *20*(4), 487–509, doi:10.1029/2000TC001226.

Edwards, M. A., W. S. F. Kidd, J. Li, Y. Yue, and M. Clark (1996), Multi-stage development of the southern Tibet detachment system near Khula Kangri: New data from Gonta La, *Tectonophysics*, *260*, 1–19, doi:10.1016/0040-1951(96)00073-X.

Eggins, S. M., R. L. Rudnick, and W. F. McDonough (1998), The composition of peridotites and their minerals: A laser ablation ICP-MS study, *Earth Planet. Sci. Lett.*, *154*, 53–71, doi:10.1016/S0012-821X(97)00195-7.

Foster, G., P. Kinny, D. Vance, C. Prince, and N. Harris (2000), The significance of monazite U-Th-Pb age data in metamorphic assemblages; a combined study of monazite and garnet chronometry, *Earth Planet. Sci. Lett.*, *181*, 327–340, doi:10.1016/S0012-821X(00)00212-0.

Fraser, G., B. Worley, and M. Sandiford (2000), High-precision geothermobarometry across the High Himalayan metamorphic sequence, Langtang Valley, Nepal, *J. Metamorph. Geol.*, *18*(6), 665–681, doi:10.1046/j.1525-1314.2000.00283.x.

Fuchs, G. (1964), Beitrag zur Kenntnis des Palaozoikums und Mesozoikums der Tibetischen Zone in Dolpo (Nepal, Himalaja), *Verh. Geol. Bundesanst.*, 1, 6–15.

Fuchs, G. (1977), The geology of the Karnali and Dolpo regions, western Nepal, *Jahrb. Geol. Bundesanst.*, *120*(2), 165–217.

Fuchs, G., and W. Frank (1970), The geology of West Nepal between the rivers Kali Gandaki and Thulo Bheri, *Jahrb. Geol. Bundesanst. Sonderb.*, *18*, 3–103.

Gaetani, M., and E. Garzanti (1991), Multicyclic history of the northern India continental margin (Northwestern Himalaya), *Am. Assoc. Pet. Geol. Bull.*, *75*, 1427–1446.

Gansser, A. (1964), *Geology of the Himalayas*, Wiley Interscience, London.

Garzanti, E., G. Vezzoli, S. Andò, J. Lavè, M. Attal, C. France-Lanord, and P. DeCelles (2007), Quantifying sand provenance and erosion (Marsyandi River, Nepal Himalaya), *Earth Planet. Sci. Lett.*, *258*, 500–515, doi:10.1016/j.epsl.2007.04.010.

Godin, L., R. L. Brown, and S. Hanmer (1999), High strain zone in the hanging wall of the Annapurna detachment, central Nepal Himalaya, in *Himalaya and Tibet: Mountain Roots to Mountain Tops*, edited by A. Macfarlane, R. Sorkhabi, and J. Quade, *Spec. Pap. Geol. Soc. Am.*, *328*, 199–210.

Godin, L., R. R. Parrish, R. L. Brown, and K. V. Hodges (2001), Crustal thickening leading to exhumation of the Himalayan metamorphic core of central Nepal: Insight from U-Pb geochronology and 40Ar/39Ar thermochronology, *Tectonics*, *20*(5), 729–747, doi:10.1029/2000TC001204.

Godin, L., D. Grujic, R. D. Law, and M. P. Searle (2006), Channel flow, ductile extrusion and exhumation in continental collision zones: An introduction, in *Channel Flow, Ductile Extrusion and Exhumation in Continental Collision Zones*, edited by R. D. Law, M. P. Searle, and L. Godin, *Geol. Soc. Spec. Publ.*, *268*, 1–23.

Goscombe, B., and M. Hand (2000), Contrasting *P-T* paths in the Eastern Himalaya, Nepal: Inverted isograds in a paired metamorphic mountain belt, *J. Petrol.*, *41*(12), 1673–1719, doi:10.1093/petrology/41.12.1673.

Goscombe, B., D. Gray, and M. Hand (2006), Crustal architecture of the Himalayan metamorphic front in eastern Nepal, *Gondwana Res.*, *10*, 232–255.

Grasemann, B., H. Fritz, and J. C. Vannay (1999), Quantitative kinematic flow analysis from the Main Central Thrust Zone (NW Himalaya, India): Implications for a decelerating strain path and the extrusion of orogenic wedges, *J. Struct. Geol.*, *21*, 837–853, doi:10.1016/S0191-8141(99)00077-2.

Gruijc, D. (2006), Channel flow and continental collision tectonics: An overview, in *Channel Flow, Ductile Extrusion and Exhumation in Continental Collision Zones*, edited by R. D. Law, M. P. Searle, and L. Godin, *Geol. Soc. Spec. Publ.*, *268*, 25–37.

Grujic, D., M. Casey, C. Davidson, L. Hollister, K. Kundig, T. Pavlis, and S. Schmid (1996), Ductile extrusion of the Higher Himalayan crystalline in Bhutan: Evidence from quartz microfabrics, *Tectonophysics*, *260*, 21–43, doi:10.1016/0040-1951(96)00074-1.

Grujic, D., L. Hollister, and R. R. Parrish (2002), Himalayan metamorphic sequence as an orogenic channel: Insight from Bhutan, *Earth Planet. Sci. Lett.*, *198*, 177–191, doi:10.1016/S0012-821X(02)00482-X.

Guillot, S. (1999), An overview of the metamorphic evolution of central Nepal, *J. Asian Earth Sci.*, *17*, 713–725.

Guillot, S., M. Cosca, P. Allemand, and P. Le Fort (1999), Contrasting metamorphic and geochronologic evolution along the Himalayan belt, in *Himalaya and Tibet: Mountain Roots to Mountain Tops*, edited by A. Macfarlane, R. Sorkhabi, and J. Quade, *Spec. Pap. Geol. Soc. Am.*, *328*, 117–128.

Guillot, S., G. Maheo, G. De Sigoyer, J. K. H. Hattori, and A. Pècher (2008), Tethyan and Indian subduction viewed from the Himalayan high- to ultra-high-pressure metamorphic rocks, *Tectonophyics*, *1–4*, 225–241, doi:10.1016/j.tecto.2007.11.059.

Harris, N., and J. Massey (1994), Decompression and anatexis of Himalayan metapelites, *Tectonics*, *13*(6), 1537–1546, doi:10.1029/94TC01611.

Harris, N., M. Ayres, and J. Massey (1995), Geochemistry of granitic melts produced during the incongruent melting of muscovite: Implications for the extraction of Himalayan leucogranite magmas, *J. Geophys. Res.*, *100*(B8), 15,767–15,777, doi:10.1029/94JB02623.

Harrison, T. M., M. Grove, O. M. Lovera, E. J. Catlos, and J. D'Andrea (1999), The origin of Himalayan anatexis and inverted metamorphism: Models and constraints, *J. Asian Earth Sci.*, *17*, 755–772, doi:10.1016/S1367-9120(99)00018-8.

Hatcher, R. D., and A. J. Merschat (2006), The Appalachian Inner Piedmont: An exhumed strike-parallel, tectonically forced orogenic channel, in *Channel Flow, Ductile Extrusion and Exhumation in Continental Collision Zones*, edited by R. D. Law, M. P. Searle, and L. Godin, *Geol. Soc. Spec. Publ.*, *268*, 517–541.

Hermann, J., and D. Rubatto (2003), Relating zircon and monazite domains to garnet growth zones: Age and duration of granulite facies metamorphism in the Val Malenco lower crust, *J. Metamorph. Geol.*, *21*, 833–852.

Hodges, K. (2000), Tectonics of Himalaya and southern Tibet from two perspectives, *Geol. Soc. Am. Bull.*, *112*, 324–350, doi:10.1130/0016-7606(2000)112<324:TOTHAS>2.0.CO;2.

Hodges, K. (2006), A synthesis of the Channel Flow-Extrusion hypothesis as developed for the Himalayan-Tibet orogenic system, in *Channel Flow, Ductile Extrusion and Exhumation in Continental Collision Zones*, edited by R. D. Law, M. P. Searle, and L. Godin, *Geol. Soc. Spec. Publ.*, *268*, 71–90.

Hodges, K. V., B. C. Burchfiel, L. H. Royden, Z. Chen, and Y. Liu (1993), The metamorphic signature of contemporaneous extension and shortening in the central Himalayan orogen: Data from the Nyalam transect, southern Tibet, *J. Metamorph. Geol.*, *11*, 721–737, doi:10.1111/j.1525-1314.1993.tb00183.x.

Hodges, K. V., R. R. Parrish, and M. P. Searle (1996), Tectonics evolution of the central Annapurna Range, Nepalese Himalayas, *Tectonics*, *15*(6), 1264–1291, doi:10.1029/96TC01791.

Hoisch, T. D. (1990), Empirical calibration of six geobarometers for the mineral assemblage quartz+muscovite+biotite+plagioclase+garnet, *Contrib. Mineral. Petrol.*, *104*(2), 225–234, doi:10.1007/BF00306445.

Holland, T., and R. Powell (1998), An internally consistent thermodynamic data set for phases of petrological interest, *J. Metamorph. Geol.*, *16*, 309–343, doi:10.1111/j.1525-1314.1998.00140.x.

Hubbard, M. S. (1989), Thermobarometric constraints of the thermal history of the Main Central Thrust zone and Tibetan Slab, eastern Nepal Himalaya, *J. Metamorph. Geol.*, *7*, 19–30, doi:10.1111/j.1525-1314.1989.tb00572.x.

Inger, S., and N. Harris (1993), Geochemical constraints on leucogranite magmatism in the Langtang Valley, Nepal Himalaya, *J. Petrol.*, *34*(2), 345–368.

Kohn, M. J. (2008), P-T-t data from Nepal support critical taper and repudiate large channel flow of the Greater Himalayan Sequence, *Geol. Soc. Am. Bull.*, *120*, 259–273, doi:10.1130/B26252.1.

Kohn, M. J., M. S. Wieland, C. D. Parkinson, and B. N. Upreti (2005), Five generations of monazite in Langtang gneisses: Implications for chronology of the Himalayan metamorphic core, *J. Metamorph. Geol.*, *120*(3/4), 259–273.

Kretz, R. (1983), Symbols for rock-forming minerals, *Am. Mineral.*, *68*, 277–279.

Larson, K., and L. Godin (2009), Kinematics of the Greater Himalayan sequence, Dhaulagiri Himal: Implications for the structural framework of central Nepal, *J. Geol. Soc.*, *166*, 25–43, doi:10.1144/0016-76492007-180.

Lee, J., B. R. Hacker, W. S. Dinklage, Y. Wang, P. Gans, A. Calvert, J. Wan, W. Chen, A. E. Blythe, and W. McClelland (2000), Evolution of the Kangmar Dome, southern Tibet: Structural, petrologic, and thermochronologic constraints, *Tectonics*, *19*(5), 872–895, doi:10.1029/1999TC001147.

Leech, M. L. (2008), Does the Karakoram fault interrupt mid-crustal channel flow in the western Himalaya?, *Earth Planet. Sci. Lett.*, *276*, 314–322, doi:10.1016/j.epsl.2008.10.006.

Le Fort, P. (1975), Himalaya: The collided range, *Am. J. Sci.*, *275A*, 1–44.

Le Fort, P. (1994), *French Earth Sciences Research in the Himalaya Regions: Kathmandu*, 174 pp., Alliance Française, Nepal.

Lombardo, B., P. C. Pertusati, and S. Borghi (1993), Geology and tectono magmatic evolution of the eastern Himalaya along Chomolungma-Makalu transect, in *Himalayan Tectonics*, edited by P. J. Treloar and M. P. Searle, *Geol. Soc. Spec. Publ.*, *74*, 341–355.

Ludwig, K. R. (2000), Isoplot/Ex version 2.4., A geochronological toolkit for Microsoft Excel, 56 pp., Berkeley Geochronol. Cen., Berkeley, Calif.

Macfarlane, A. M. (1993), Chronology of tectonic events in crystalline core of the Himalaya, Langtang National Park, Central Nepal, *Tectonics*, *12*(4), 1004–1025, doi:10.1029/93TC00916.

Macfarlane, A. M. (1995), An evaluation of the inverted metamorphic gradient at Lantang National Park, central Nepal Himalaya, *J. Metamorph. Geol.*, *13*, 595–612, doi:10.1111/j.1525-1314.1995.tb00245.x.

Maruo, Y., and K. Kizaki (1983), Thermal structure in the nappes of the eastern Nepal Himalayas, in *Granites of Himalayas, Karakorum and Hindu Kush*, edited by F. A. Shams, pp. 271–286, Inst. of Geol., Punjab Univ., Lahore, Pakistan.

Meldrum, A., L. A. Boatner, W. J. Weber, and R. C. Wewing (1998), Radiation damage in zircon and monazite, *Geochim. Cosmochim. Acta*, *62*, 2509–2520, doi:10.1016/S0016-7037(98)00174-4.

Najman, Y., et al. (2008), The Paleogene record of Himalayan erosion: Bengal Basin, Bangladesh, *Earth Planet. Sci. Lett.*, *273*(1–2), 1–14, doi:10.1016/j.epsl.2008.04.028.

Passchier, C. W., and R. J. Trouw (1996), *Microtectonics*, 289 pp., Springer Verlag, Berlin.

Pattison, D. R. M. (1992), Stability of andalusite and sillimanite and the Al2SiO5 triple point: Constraints trom the Ballachulish aureole, Scotland, *J. Geol.*, *100*, 423–446, doi:10.1086/629596.

Pearce, N. J. G., W. T. Perkins, J. A. Westgate, M. P. Gorton, S. E. Jackson, C. R. Neal, and S. P. Chenery (1997), A compilation of new and published major and trace element data for NIST SRM 610 and NIST SRM 612 glass reference materials, *Geostand. Newsl.*, *21*, 115–144, doi:10.1111/j.1751-908X.1997.tb00538.x.

Pidgeon, R. T. (1992), Recrystallisation of oscillatory zoned zircon: Some geochronological and petrological implications, *Contrib. Mineral. Petrol.*, *110*(4), 463–472, doi:10.1007/BF00344081.

Pognante, U., and P. Benna (1993), Metamorphic zonation, migmatization, and leucogranites along the Everest transect of Eastern Nepal and Tibet: Record of an exhumation history, in *Himalayan Tectonics*, edited by P. J. Treloar and M. P. Searle, *Geol. Soc. Spec. Publ.*, *74*, 328–340.

Reddy, M. S., M. P. Searle, and J. A. Massey (1993), Structural evolution of the High Himalayan Gneiss sequence, in *Himalayan Tectonics*, edited by P. J. Treloar and M. P. Searle, *Geol. Soc. Spec. Publ.*, *74*, 374–389.

Robinson, D. M., P. G. De Celles, C. N. Garzione, O. N. Pearson, T. M. Harrison, and E. J. Catlos (2003), Kinematic model for the Main Central Thrust in Nepal, *Geology*, *31*, 339–362, doi:10.1130/0091-7613(2003)031<0359:KMFTMC>2.0.CO;2.

Robinson, D. M., P. G. De Celles, and P. Copeland (2006), Tectonic evolution of the Himalayan thrust belt in western Nepal: Implications for channel flow models, *Geol. Soc. Am. Bull.*, *118*, 865–885, doi:10.1130/B25911.1.

Rubatto, D., J. Hermann, and I. S. Buick (2006), Temperature and bulk composition control on the growth of monazite and zircon during low-pressure anatexis (Mount Stafford, Central Australia), *J. Petrol.*, *47*(10), 1973–1996, doi:10.1093/petrology/egl033.

Scaillet, B., M. Pichavant, and J. Roux (1995), Experimental crystallization of leucogranite magmas, *J. Petrol.*, *36*, 663–705.

Schelling, D. (1999), Geological map of the eastern Nepal Himalaya, *J. Asian Earth Sci.*, *17*(5–6), AD9–AD20.

Searle, M. P. (1999), Extensional and compressional faults in the Everest-Lhotse Massif, Khumbu Himalaya, Nepal, *J. Geol. Soc.*, *156*, 227–240, doi:10.1144/gsjgs.156.2.0227.

Searle, M. P., and L. Godin (2003), The South Tibetan Detachment System and the Manaslu leucogranite: A structural reinterpretation and restoration of the Annapurna-Manaslu Himalaya, Nepal, *J. Geol.*, *111*, 505–524, doi:10.1086/376763.

Spear, F. S. (1993), *Metamorphic Phase Equilibria and Pressure-Temperature-Time Paths*, Mineral. Soc. of Am., Washington, D.C.

Spear, F. S., M. J. Kohn, and J. Cheney (1999), P-T paths from anatectic pelites, *Contrib. Mineral. Petrol.*, *134*, 17–32, doi:10.1007/s004100050466.

Swapp, S. M., and L. S. Hollister (1991), Inverted metamorphism within the Tibetan slab of Bhutan: Evidence for a tectonically transported heat source, *Can. Mineral.*, *29*, 1019–1041.

Thompson, A. B. (1996), Fertility of crustal rocks during anatexis, *Trans. R. Soc. Edinburgh Earth Sci.*, *87*, 1–10.

Treloar, P. J., R. D. Broughton, M. P. Williams, M. P. Coward, and B. F. Windley (1989), Deformation, metamorphism and imbrication of the Indian plate, south of the Main Mantle thrust, north Pakistan, *J. Metamorph. Geol.*, *7*, 111–125, doi:10.1111/j.1525-1314.1989.tb00578.x.

Upreti, B. N. (1999), An overview of the stratigraphy and tectonics of the Nepal Himalaya, *J. Asian Earth Sci.*, *17*, 577–606, doi:10.1016/S1367-9120(99)00047-4.

Vannay, J. C., and K. Hodges (1996), Tectonometamorphic evolution of the Himalayan metamorphic core between the Annapurna and Dhaulagiri, central Nepal, *J. Metamorph. Geol.*, *14*, 635–656, doi:10.1046/j.1525-1314.1996.00426.x.

Viskupic, K., K. Hodges, and S. A. Bowring (2005), Timescales of melt generation and the thermal evolution of the Himalayan metamorphic core, Everest region, eastern Nepal, *Contrib. Mineral. Petrol.*, *149*, 1–21, doi:10.1007/s00410-004-0628-5.

Wei, C. J., R. Powell, and G. L. Clarke (2004), Calculated phase equilibria for low- and medium-pressure metapelites in the KFMASH and KMnFMASH systems, *J. Metamorph. Geol.*, *22*, 495–508, doi:10.1111/j.1525-1314.2004.00530.x.

White, N. M., M. Pringle, E. Garzanti, M. Bickle, Y. Najman, H. Chapman, and P. Friend (2002), Constraints on the exhumation and erosion of the High Himalayan Slab, NW India, from foreland basin deposits, *Earth Planet. Sci. Lett.*, *195*, 29–44, doi:10.1016/S0012-821X(01)00565-9.

Williams, I. (1998), U-Th-Pb geochronology by ion microprobe, *Rev. Econ. Geol.*, *7*, 1–35.

Wobus, C. W., K. X. Whipple, and K. V. Hodges (2006), Neotectonics of the central Nepalese Himalaya: Constraints from geomorphology, detrital $^{40}Ar/^{39}Ar$ thermochronology, and thermal modeling, *Tectonics*, *25*(4), TC4011, doi:10.1029/2005TC001935.

Yin, A. (2006), Cenozoic tectonic evolution of the Himalayan orogen as constrained by along-strike variation of structural geometry, exhumation history, and foreland sedimentation, *Earth Sci. Rev.*, *76*, 11–131, doi:10.1016/j.earscirev.2005.05.004.

R. Carosi and C. Montomoli, Dipartimento di Scienze della Terra, University of Pisa, Via S. Maria 53, Pisa 56126, Italy. (carosi@dst.unipi.it)

D. Rubatto, Research School of Earth Sciences, Australian National University, Canberra 0200, Australia.

D. Visonà, Dipartimento di Geoscienze, University of Padova, Via Matteotti 32, Padova 35122, Italy.